Mon. Not. R. Astron. Soc. **302,** 222–244 (1999)

A deep VLA survey at 20 cm of the *ISO* ELAIS survey regions

P. Ciliegi,[1,2⋆†] R. G. McMahon,[1†] G. Miley,[3] C. Gruppioni,[4] M. Rowan-Robinson,[4] C. Cesarsky,[5] L. Danese,[6] A. Franceschini,[7] R. Genzel,[8] A. Lawrence,[9] D. Lemke,[10] S. Oliver,[4] J.-L. Puget[11] and B. Rocca-Volmerange[11,12]

[1] *Institute of Astronomy, University of Cambridge, Madingley Road, Cambridge CB3 0HA*
[2] *Osservatorio Astronomico di Bologna, via Zamboni 33, I-40126 Bologna, Italy*
[3] *Leiden Observatory, PO Box 9513, 2300 RA Leiden, the Netherlands*
[4] *Astrophysics Group, Imperial College, Blackett Laboratory, Prince Consort Road, London SW7 2BZ*
[5] *Service d'Astrophysique, Saclay, F-91191 Gif-sur-Yvette, France*
[6] *SISSA, Via Beirut 2–4, Trieste, Italy*
[7] *Osservatorio Astronomico di Padova, Vicolo dell'Osservatorio 5, I-35122 Padova, Italy*
[8] *Max-Planck-Institut für Extraterrestrische Physik, Giessenbachstrasse, D-8046 Garching bei Munchen, Germany*
[9] *Institute for Astronomy, University of Edinburgh Blackford Hill, Edinburgh EH9 3HJ*
[10] *Max-Plank-Institut für Astronomie, Körnigstuhl 17, D-69117 Heidelberg, Germany*
[11] *Institut d'Astrophysique Spatiale, Bat. 121, Université Paris XI, F-91405 Orsay, France*
[12] *Institut d'Astrophysique de Paris, CNRS, 98 bis Bd. Arago, F-75014 Paris, France*

Accepted 1998 September 2. Received 1998 August 24; in original form 1998 June 5

ABSTRACT

We have used the Very Large Array (VLA) in C configuration to carry out a sensitive 20-cm radio survey of regions of sky that have been surveyed in the far-infrared (FIR) over the wavelength range 5–200 μm with *ISO* (*Infrared Space Observatory*) as part of the European Large-Area *ISO* Survey (ELAIS). As usual in surveys based on a relatively small number of overlapping VLA pointings, the flux limit varies over the area surveyed: from a 5σ limit of 0.135 mJy over an area of 0.12 deg^2 to 1.15 mJy or better over the whole region covered of 4.22 deg^2. In this paper we present the complete radio catalogue of 867 sources, 428 of which form a complete sample in the flux range 0.2–1.0 mJy. These regions of sky have previously been surveyed to shallower flux limits at 20 cm with the VLA as part of the VLA D configuration NVSS (full width at half-maximum, FWHM = 45 arcsec) and VLA B configuration FIRST (FWHM = 5 arcsec) surveys. Our whole survey has a nominal 5σ flux limit a factor of 2 below that of the NVSS; 3.4 deg^2 of the survey reaches the nominal flux limit of the FIRST survey and 1.5 deg^2 reaches 0.25 mJy, a factor of 4 below the nominal FIRST survey limit. In addition, our survey is at a resolution intermediate between the two surveys and thus is well suited for a comparison of the reliability and resolution-dependent surface brightness effects that affect interferometric radio surveys. We have carried out a detailed comparison of our own survey and these two independent surveys in order to assess the reliability and completeness of each. Considering the whole sample, we found that to the 5σ nominal limits of 2.3 and 1.0 mJy, respectively, the NVSS and FIRST surveys have a completeness of 96^{+2}_{-3} and 89^{+2}_{-3} per cent and a reliability of 99^{+1}_{-2} and 94^{+2}_{-2} per cent.

Key words: surveys – radio continuum: galaxies – radio continuum: general.

1 INTRODUCTION

The *Infrared Space Observatory* (*ISO*) (Kessler et al. 1996), launched in 1995 November, was the successor to the *Infrared Astronomical Satellite* (*IRAS*) and provided unparalleled sensitivity at mid- to far-infrared wavelengths (i.e. 5–200 μm). The European Large-Area *ISO* Survey (ELAIS) (Oliver et al. 1997; Oliver et al., in preparation) is a project that used *ISO* to carry out a deep wide-angle survey at wavelengths of 6.7, 15, 90 and 175 μm. The 6.7- and 15-μm surveys employed the *ISO*-CAM camera (Cesarsky et al. 1996) with the aim to reach a 5σ sensitivity of ∼2 mJy at 15 μm. The 90- and 175-μm surveys used the *ISO*-PHOT camera (Lemke

⋆Present address: Osservatorio Astronomico di Bologna, Viale Berti-Pichat 6, I-40127 Bologna, Italy.
†E-mail: ciliegi@astbo3.bo.astro.it (PC); rgm@ast.cam.ac.uk (RGM)

et al. 1994) with the aim to reach a 5σ sensitivity of $\sim$25 mJy. At these limits, we expect *ISO* to be confusion-limited at 90 and 175 μm by galaxies and Galactic cirrus emission, and hence this survey should be the deepest FIR survey possible with the satellite.

The area covered in the ELAIS survey is $\sim$13 deg^2 at 15 and 90 μm, $\sim$7 deg^2 at 6.7 μm and $\sim$3 deg^2 at 175 μm.

The ELAIS survey is $\sim$50 times deeper at 5–20 μm than *IRAS*. Thus our survey will allow us to explore *IRAS*-like populations to higher redshift and possibly unveil new classes of objects or unexpected phenomena. We expect to detect thousands of galaxies, many of which will be at high redshifts and undergoing vigorous star formation. The expected large number of high-z IR galaxies should provide vital information about the star formation rate out to $z = 1$ and possibly earlier.

The spatial resolution of *ISO* will be insufficient to identify optically faint objects properly. At 15 μm, the survey resolution (full width at half-maximum, FWHM) is $\sim$10 arcsec and at 90 μm it is about 1 arcmin. Complementary radio data will play a crucial role in identifying many of the most interesting objects, as they did in the early days of X-ray astronomy (e.g. Cyg X-1) and in more recent times for *IRAS* (e.g. IRAS F10214+4714; Rowan-Robinson et al. 1991).

In this paper we report the description of the radio observations obtained in the three *ISO* ELAIS survey regions in the Northern celestial hemisphere (N1_1610+5430, N2_1636+4115 and N3_1429+3306). The observations are made with the Very Large Array (VLA) radio telescope at 1.4 GHz (20 cm) in the VLA C configuration (maximum baseline 3.4 km) with a resolution (FWHM) of $\sim$15 arcsec. The aim of these VLA observations was to obtain uniform coverage of the ELAIS regions with an rms noise limit of $\sim$50 μJy. These VLA observations will be essential in the optical identification phase of the ELAIS sources and in assessing the reliability of the ELAIS source lists.

Moreover, with a radio survey it will be possible to investigate the radio/far-infrared correlation in star-forming galaxies to flux densities considerably fainter than those reached by *IRAS*. Helou, Soifer & Rowan-Robinson (1985) noted a strong correlation between radio and far-infrared flux for star-forming galaxies, valid over a very wide range of infrared luminosities, a result that has been confirmed in many subsequent studies (e.g. Wunderlich, Klein & Wielebinski 1987; Condon, Anderson & Helou 1991). The radio emission is interpreted as a synchrotron radiation from relativistic electrons that have leaked out of supernova remnants. It is expected that this correlation should extend below the *IRAS* flux level since the majority of sub-mJy radio sources have been identified with faint blue galaxies with spectra similar to those of star-forming objects (Benn et al. 1993).

In addition, combining deep radio and optical data with the *ISO* survey fluxes will provide information on the trivariate IR–radio–optical luminosity function and its evolution, and the contribution of starburst galaxies to the sub-mJy radio source counts. The ratio of the FIR emission and radio emission will also allow us to investigate the physical origin and spatial distribution of the energy sources in the detected objects in the same way that VLA maps have been central to our understanding of the origin of *IRAS* sources.

Finally, owing to its depth and angular extension, this survey is important also as a radio survey in its own right. In fact, the selected sample is large and deep enough to constitute a statistically significant sample of sub-mJy radio sources, whose nature and characteristics are still a major topic in observational cosmology (see Windhorst, Mathis & Neuschaefer 1990; Fomalont et al. 1991; Rowan-Robinson et al. 1993; Gruppioni et al. 1997).

The *ISO* ELAIS survey is available at http://athena.ph.ic.ac.uk.

2 RADIO OBSERVATIONS

2.1 Choice of observing frequency and VLA configuration

The VLA C configuration and the observing frequency of 1.4 GHz give the optimum resolution to acquire the kind of radio data that we need. The VLA D configuration is confusion-limited at the fluxes we wish to attain (the 5σ confusion limit in D configuration is 0.4 mJy/beam). With the C configuration and a frequency of 1.4 GHz the synthesized beam size (full width at half-power, FWHP) is $\sim$15

Table 1. VLA observations of ELAIS regions.

Region	Pointing	Observing data	RA (J2000)	Dec. (J2000)	Integration time (min)	Theoretical rms (mJy)	Observed rms (mJy)
N1	V1	April 96	16 10 00.0	+54 30 00	58.4	0.052	0.049
N1	V1	July 97	16 10 00.0	+54 30 00	175.4	0.030	0.030
N1	V2	July 97	16 09 25.5	+54 06 32	57.8	0.052	0.050
N1	V3	July 97	16 07 34.6	+54 25 05	58.5	0.052	0.051
N1	V4	July 97	16 08 09.6	+54 49 08	59.5	0.052	0.052
N1	V5	July 97	16 10 37.8	+54 54 36	59.0	0.052	0.049
N1	V6	July 97	16 12 28.4	+54 35 55	59.0	0.052	0.051
N1	V7	July 97	16 11 51.2	+54 11 54	57.8	0.052	0.052
N2	V1	April 96	16 36 00.0	+41 06 00	65.3	0.050	0.050
N2	V2	April 96	16 34 00.0	+41 06 00	56.8	0.053	0.052
N2	V3	April 96	16 38 00.0	+41 06 00	59.3	0.052	0.050
N2	V4	July 97	16 37 00.0	+40 46 00	59.2	0.052	0.052
N2	V5	July 97	16 37 00.0	+41 26 00	59.0	0.052	0.052
N2	V6	July 97	16 35 00.0	+40 46 00	59.5	0.052	0.053
N2	V7	July 97	16 35 00.0	+41 26 00	59.5	0.052	0.051
N2	VD	July 97	16 35 00.0	+41 06 00	178.4	0.030	0.032
N3	V1	April 96	14 28 30.0	+33 20 00	56.5	0.053	0.053
N3	V2	April 96	14 26 30.0	+33 20 00	58.7	0.052	0.053
N3	V3	July 97	14 27 30.0	+32 58 30	58.9	0.052	0.052
N3	V4	July 97	14 30 30.0	+33 20 00	59.5	0.052	0.050
N3	V5	July 97	14 29 30.0	+32 58 30	58.0	0.052	0.051

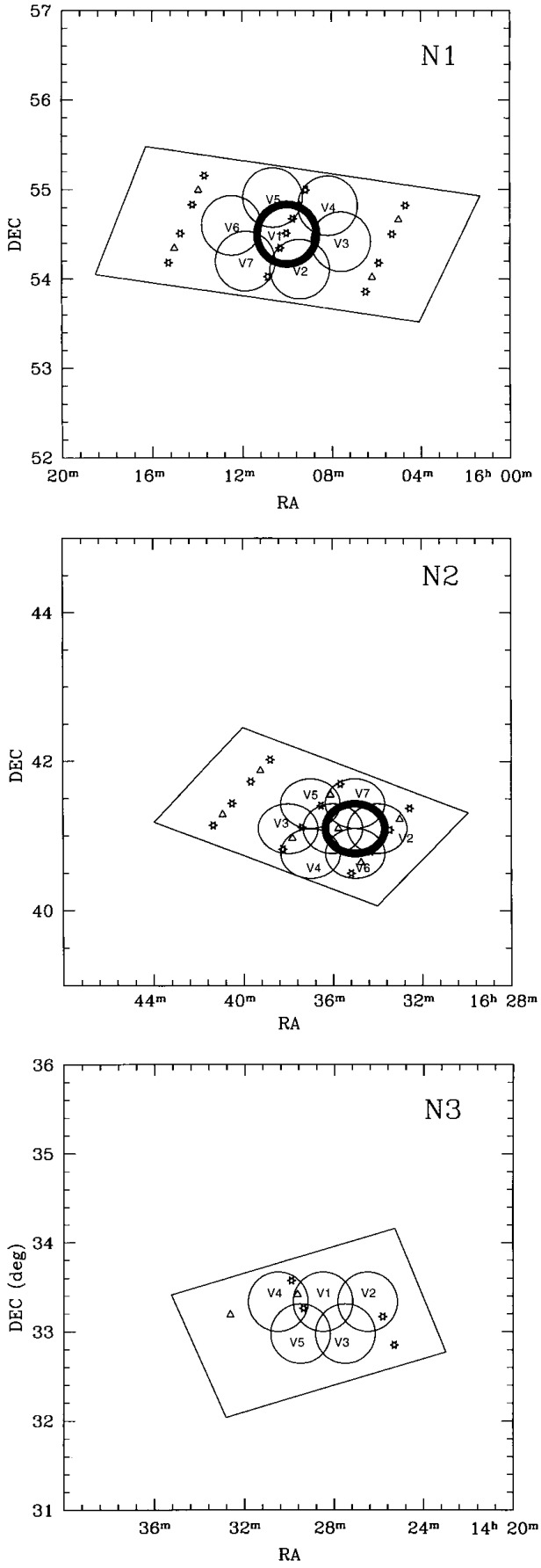

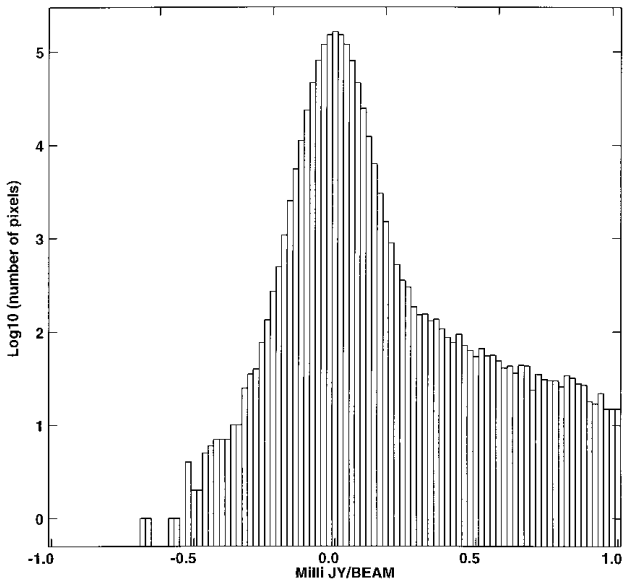

Figure 2. Logarithmic histogram of VLA map peak flux densities in the pointing N2 V1.

arcsec, which should enable us to pinpoint optical identifications to ~1–2 arcsec, except for asymmetric multicomponent sources. The frequency of 1.4 GHz was chosen because at this frequency the FWHP of the VLA primary beam is 31 arcmin. This allows us to cover the ELAIS survey fields with a relatively small number of pointing centres. It is possible to obtain a mosaic map with nearly uniform sensitivity if the separation is $31/\sqrt{2} \sim 22$ arcmin. Moreover, at 1.4 GHz there will be contributions from both the steep and flat spectrum populations of radio sources.

Our observations are made in spectral line mode using two different IF (intermediate frequency) channels centred at 1.3649 GHz (IF1) and 1.4352 GHz (IF2). Each IF channel has a bandwidth of 18.75 MHz, which is subdivided into seven spectral line channels evenly spaced in frequency across the bandwidth of the input IF channel. Therefore, we have a total of 14 spectral line channels with a bandwidth of 2.68 MHz each. We decided to use the line mode in order to facilitate wide-field mapping and avoid the effect of interference. The total bandwidth available is thus 37.5 MHz, narrower than the 2×50 MHz used in continuum mode. A narrower bandwidth means a worse sensitivity. In our case we lose about 30 per cent in signal-to-noise ratio near the pointing centres because the total bandwidth is ~40 per cent of that in the continuum mode. However, we reduce the chromatic aberration (bandwidth smearing) considerably, which reduces the area covered by each pointing in continuum mode. In addition, the line mode is less susceptible to narrow-band interference, since one only needs to excise the channel that is affected rather than losing the whole IF band, which is the case in continuum mode. Since our aim is to obtain a uniform sensitivity over the whole ELAIS fields and not to obtain a single-field deep survey, we have opted to use the line mode.

Figure 1. The sky position and orientation of the *ISO* survey regions. Each outer rectangle is 120×80 arcmin^2. The triangles show the *ISO*-CAM pointings, while the asterisks show the *ISO*-PHOT pointings. The circles show the regions we mapped with the VLA. The circles are drawn with radii $R = 20$ arcmin, where the VLA power sensitivity is ~30 per cent of the central value. The thick circles in N1 and N2 show the location of the deep pointings (see text for more details).

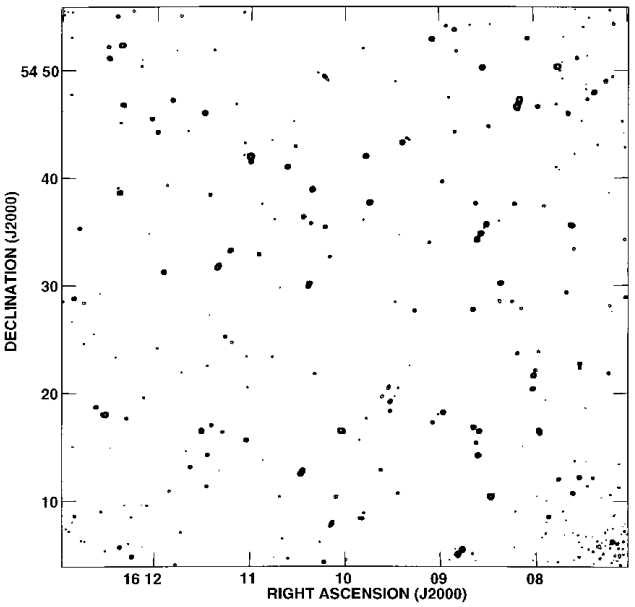

Figure 3. Central 52×52 arcmin^2 $= 1040 \times 1040$ pixels of the mosaic map N1. The contour levels are 0.25, 0.50, 0.75, 1.00, 1.25,... mJy. The noise at the corners of the image (see for example the lower right corner) is the result of the increase of the rms noise as the off-axis angle increases.

Moreover, the reduced bandwidth smearing in line mode will give us more accurate angular sizes for our sources.

2.2 Observations

The VLA observation of the ELAIS regions were carried out in 1996 April (10 h) and in 1997 July (24 h). A total of 20 pointings were made in 20-cm spectral line mode. Seven of these pointings are in the ELAIS field N1, eight in the field N2 and five in N3. The integration time of each pointing was ∼1 h. This allowed us to obtain, at each field centre, an rms noise of ∼0.05 mJy (a 5σ limit of 0.25 mJy). Moreover, during the 1997 July run, we observed two regions (one in N1 and one in N2) with an integration time of ∼3 h each. In particular, in N1 we re-observed (for ∼3 h) the pointing V1 (already observed for 1 h in 1996 April) while in N2 the deep pointing (N2 VD) was shifted 10 arcmin from the map centre to avoid the presence of a strong (>100 mJy) radio source. In the two deep pointings N1 V1 and N2 VD we reached an rms noise of ∼0.026 mJy (a 5σ limit of 0.13 mJy). Finally, in order to study the degradation of the image quality as a function of the off-axis angle, a strong calibrator (the source 3C 286) was observed at position offsets of 5, 10, 15, 20, 25, 30 and 35 arcmin in two orthogonal directions (north–south and east–west). The result of this test is reported in Section 5.1.2.

In Table 1, we report the position of the centre of each observation, while Fig. 1 shows the sky positions and orientations

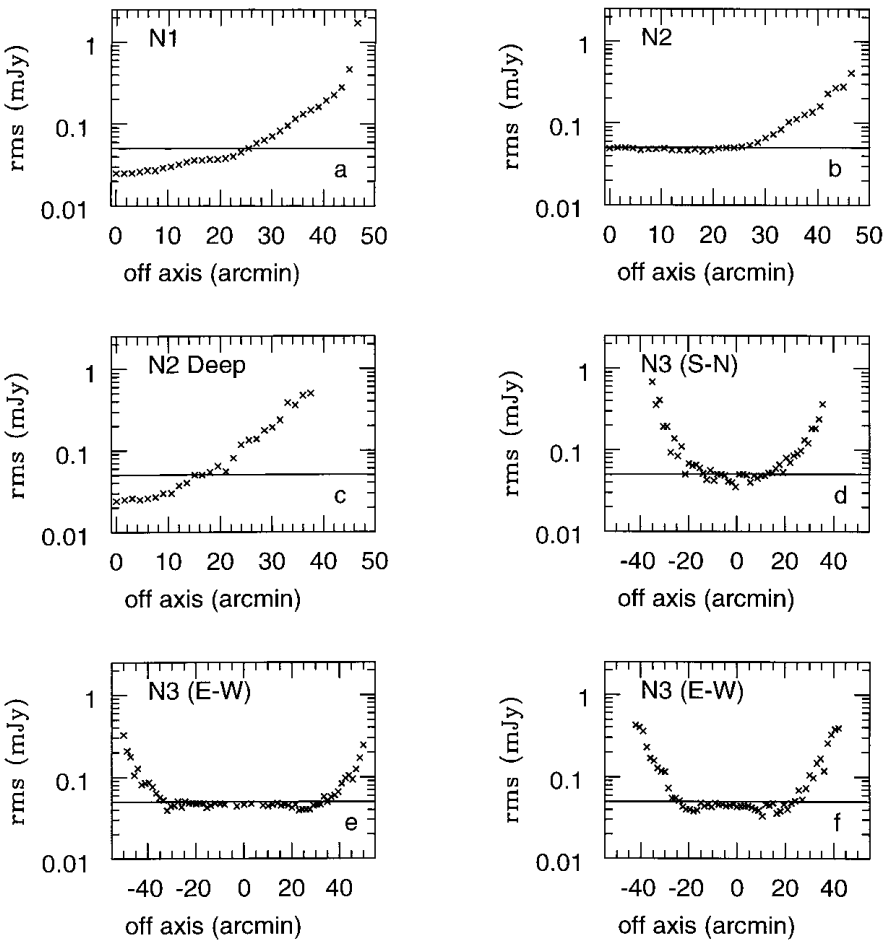

Figure 4. The rms noise value as a function of the off-axis value. The solid line represent an rms value of 0.05 mJy. See text for more details.

of the *ISO* survey regions. The circles show the VLA regions mapped. The circles are drawn with a radius ($R \sim 20$ arcmin) where the VLA power sensitivity is ~30 per cent of the central value.

3 DATA REDUCTION

All the data were analysed with the NRAO AIPS reduction package. The data were calibrated using 3C 286 as primary flux density calibrator [assuming a flux density of 15.04 Jy at 1.3649 GHz (IF1) and 14.70 Jy at 1.4352 GHz (IF2)], and the sources 1549+506 and 1635+381 as secondary calibrators. The task UVFLAG was used to 'flag' (delete) the corrupted data (e.g. bad integration, non-operating antennas, high amplitudes caused by interference, etc.) while the tasks VLACALIB and GETJY were used to calibrate the data and to determine the source flux densities. Finally each observation was cleaned using the task IMAGR. The cleaning procedure was stopped when the rms map noise was similar to the expected value (see below).

3.1 Rms map noise of the single pointings

The integration times of each observation after deletion of the corrupted data are reported in Table 1. The rms noise of each pointing was estimated using the amplitude distribution of the pixel values in the cleaned map before correcting for primary-beam attenuation. In Fig. 2 we show this distribution for the pointing N2 V1. This distribution is the sum of a Gaussian noise core with a positive-going tail caused by discrete sources. Note that the *y*-axis in Fig. 2 is logarithmic.

Thus, the rms of the noise distribution alone should be nearly equal to the rms of that distribution obtainable by reflecting the negative flux portion of the observed amplitude distribution about flux = 0. In column 7 of Table 1 we report the theoretical rms noise level (at 1σ) as computed directly from the observing parameters (integration time, number of antennas, observing frequency, bandwidth and number of IF channels), while in column 8 we report the 1σ rms noise level obtained by fitting the noise distribution of each pointing. As shown in Table 1 there is a very good agreement between the observed and the theoretical rms noise levels.

3.2 Mosaic maps

Using the AIPS tasks LGEOM, HGEOM and LTESS, we have combined all the observations, creating a mosaic map for each field (N1, N2 and N3). A special procedure has been adopted for N2. The presence of a deep observation not in the centre of the radio map (see above and Fig. 1) makes the noise of this map highly non-uniform. To simplify source extraction, we have created two different mosaic maps. In the first map we have combined all the observations in N2 excluding the deep pointing, while in the second one we have combined the deep pointing N2 VD with all the surrounding pointings (N2 V1, N2 V2, N2 V6 and N2 V7, see Fig. 1). In this way we have obtained two mosaic maps with smoothly varying noise: lower in the map centre and higher in the outer regions.

An example of our images is given in Fig. 3 where we show the contour map of the central region (52×52 arcmin^2) of the mosaic map N1.

3.3 Noise of the mosaic maps

We analysed the noise properties in each mosaic map (N1, N2, N2 Deep and N3). As expected, N1, N2 and N2 Deep have a regular noise distribution: a circular central region with a flat noise distribution surrounded by concentric annular regions, where the noise increases for increasing distance from the centre. No structures or irregularities were found in the rms noise maps. In Fig. 4 we plot the variation of the rms noise as a function of the off-axis angle for N1, N2 and N2 Deep. Owing to the different number of pointings in N3 (five pointings instead of seven, see Fig. 1) the mosaic map in this field has a different shape and the noise distribution in the map has a semicircular shape instead of a circular one. In Figs 4(d)–(f) we plot the variation of the rms value in three different slices. In Fig. 4(d) we plot the rms value in the north–south direction, in Fig. 4(e) the rms value in a slice that connects the centre of the three northern pointings (N3 V1, N3 V2 and N3 V4), and in Fig. 4(f) the rms value in a slice that connects the centre of the two southern pointings (N3 V3 and N3 V5). As for N1 and N2, no structures or irregularities were found in the rms noise map of N3.

4 SOURCE EXTRACTION

4.1 Regions for the source extraction

Using Fig. 4 we determined the regions with constant rms noise to be used for the source extraction. Because of the circular shape of the rms map, we searched for radio sources in a circular central region plus concentric annular regions to an off-axis value of 42 arcmin. Outside this area, the beam attenuation significantly increases the limiting flux (see Fig. 4). In each region the rms noise used for source extraction is the highest rms in the region. In this way we are sure that all the sources extracted are above the fixed threshold in the region (for example five times the rms value). The sizes of these regions are reported in Table 2 and in Fig. 5.

Table 2. The regions used for the source extraction.

Region	R_{inn} (arcmin)	R_{out} (arcmin)	Size (deg^2)	Total (deg^2)	Rms (mJy)	5σ limit (mJy)
N1						
1	0	8	0.0559	0.0559	0.027	0.135
2	8	14	0.1151	0.1710	0.034	0.170
3	14	22	0.2513	0.4223	0.038	0.190
4	22	26	0.1677	0.5900	0.050	0.250
5	26	30	0.1955	0.7855	0.070	0.350
6	30	34	0.2234	1.0089	0.100	0.500
7	34	38	0.2513	1.2602	0.150	0.750
8	38	42	0.2793	1.5395	0.230	1.150
N2						
1	0	26	0.5900	0.5900	0.050	0.250
2	26	30	0.1955	0.7855	0.070	0.350
3	30	34	0.2234	1.0089	0.100	0.500
4	34	38	0.2513	1.2602	0.150	0.750
5	38	42	0.2793	1.5395	0.230	1.150
N2 D						
1	0	8	0.0559	0.0559	0.027	0.135
2	8	11	0.0497	0.1056	0.030	0.150
3	11	14	0.0655	0.1711	0.038	0.190
N3						
1	0	26	0.2950	0.2950	0.050	0.250
2	26	30	0.1645	0.4595	0.070	0.350
3	30	34	0.1961	0.6556	0.100	0.500
4	34	38	0.2279	0.8835	0.150	0.750
5	38	42	0.2597	1.1432	0.230	1.150

Table 3. The VLA radio catalogue of the ISO regions N1, N2 and N3.

Name	S_P (mJy)	σ_{S_P} (mJy)	S_I (mJy)	σ_{S_I} (mJy)	RA (J2000)	Dec. (J200)	σ_α (arcsec)	σ_δ (arcsec)	θ_M (arcsec)	θ_m (arcsec)	PA (deg)	σ_{θ_M} (arcsec)	$\sigma\theta_m$ (arcsec)	σ_{PA} (deg)	Off-axis (arcmin)
ELAISR20 J142529+331644	1.145	0.057	1.272	0.064	14 25 29.33	+33 16 44.2	0.84	0.88	15.959	13.577	−2.2	0.801	0.681	0.2	37.9
ELAISR20 J142529+332324	0.829	0.056	0.955	0.065	14 25 29.88	+33 23 24.7	1.28	0.97	17.910	12.515	70.1	1.219	0.852	0.1	37.8
ELAISR20 J142532+330126	7.325	0.089	8.049	0.097	14 25 32.71	+33 01 26.0	0.52	0.39	15.582	13.752	108.7	0.188	0.166	0.1	41.5
ELAISR20 J142536+331600	1.855	0.054	2.309	0.068	14 25 36.55	+33 16 00.7	0.67	0.57	16.556	14.659	−52.1	0.484	0.429	0.2	36.5
ELAISR20 J142544+333704	1.399	0.095	1.317	0.090	14 25 44.80	+33 37 04.5	1.21	0.86	16.427	11.240	78.7	1.121	0.767	0.1	38.5
ELAISR20 J142552+331823	0.726	0.043	0.640	0.038	14 25 52.07	+33 18 23.6	1.00	0.77	14.816	11.592	84.5	0.878	0.687	0.2	33.0
ELAISR20 J142606+333038	1.959	0.045	3.490	0.081	14 26 06.18	+33 30 37.9	0.68	0.53	21.413	16.224	−69.3	0.496	0.376	0.1	31.8
ELAISR20 J142610+330008	1.212	0.053	1.610	0.070	14 26 10.92	+33 00 08.4	0.88	0.75	17.058	15.186	84.6	0.739	0.658	0.3	35.2
ELAISR20 J142612+333113	4.870	0.053	6.300	0.069	14 26 12.14	+33 31 13.8	0.52	0.39	18.000	14.015	61.6	0.197	0.153	0.4	30.9
ELAISR20 J142613+325535	1.063	0.053	1.402	0.070	14 26 13.63	+32 55 35.1	0.90	0.91	17.157	14.990	−21.1	0.851	0.743	0.3	37.6
ELAISR20 J142616+330922	1.948	0.027	2.096	0.029	14 26 16.76	+33 09 22.8	0.53	0.40	15.447	13.583	50.6	0.216	0.190	0.1	29.8
ELAISR20 J142619+332006	0.806	0.016	2.677	0.052	14 26 19.60	+33 20 05.8	0.92	0.50	41.726	15.521	75.3	0.803	0.299	0.5	27.2
ELAISR20 J142624+332015	1.393	0.024	1.941	0.033	14 26 24.84	+33 20 15.6	0.57	0.45	17.326	15.686	−66.4	0.298	0.270	0.1	26.1
ELAISR20 J142626+332147	0.484	0.024	0.696	0.034	14 26 26.21	+33 21 47.0	0.89	0.99	19.916	14.078	26.3	0.969	0.685	0.1	25.9
ELAISR20 J142629+332005	1.792	0.018	2.203	0.022	14 26 29.08	+33 20 05.2	0.51	0.38	16.569	14.468	85.3	0.168	0.147	0.1	25.3
ELAISR20 J142633+333211	5.102	0.077	7.516	0.113	14 26 33.55	+33 32 11.8	0.55	0.43	16.952	16.945	103.7	0.254	0.254	1.5	27.2
ELAISR20 J142639+331839	3.387	0.019	3.876	0.022	14 26 39.04	+33 18 39.7	0.49	0.36	15.597	14.306	−87.3	0.087	0.080	0.5	23.2
ELAISR20 J142640+331505	0.364	0.019	0.407	0.021	14 26 40.24	+33 15 05.8	1.12	0.69	19.266	11.314	85.1	1.010	0.593	0.1	23.5
ELAISR20 J142647+331921	0.424	0.018	0.541	0.023	14 26 47.33	+33 19 21.2	0.80	0.78	16.609	14.987	18.0	0.700	0.631	0.3	21.5
ELAISR20 J142649+325410	1.178	0.038	1.346	0.043	14 26 49.29	+32 54 10.4	0.71	0.57	16.154	13.793	−75.7	0.518	0.442	0.1	33.3
ELAISR20 J142650+332940A	9.921	0.061	9.712	0.060	14 26 50.63	+33 29 42.6	0.49	0.36	14.725	12.963	77.4	0.091	0.080	0.5	22.9
ELAISR20 J142650+332940B	1.430	0.060	1.453	0.061	14 26 48.91	+33 29 26.7	0.75	0.71	14.725	13.456	3.3	0.619	0.565	0.3	23.1
ELAISR20 J142650+332940T	9.921	0.009	11.045	0.090	14 26 50.41	+33 29 40.6	0.49	0.35	-	-	-	-	-	-	23.0
ELAISR20 J142652+330051	1.096	0.027	1.231	0.030	14 26 52.22	+33 00 51.4	0.60	0.51	15.854	13.814	−39.0	0.386	0.336	0.1	28.0
ELAISR20 J142654+332851	0.603	0.055	0.735	0.067	14 26 54.34	+33 28 51.5	1.92	1.12	20.432	11.622	85.1	1.859	1.057	0.1	21.8
ELAISR20 J142657+331815	0.400	0.015	0.564	0.022	14 26 57.64	+33 18 15.7	0.90	0.78	22.214	15.329	−51.7	0.848	0.585	0.1	19.4
ELAISR20 J142658+333312	2.516	0.078	3.534	0.110	14 26 58.85	+33 33 12.1	0.71	0.62	16.659	16.443	−72.6	0.519	0.512	1.7	23.2
ELAISR20 J142701+325935	0.964	0.027	1.069	0.030	14 27 01.31	+32 59 35.4	0.68	0.49	17.327	12.477	86.9	0.482	0.347	0.1	27.6
ELAISR20 J142701+330049	0.533	0.024	0.650	0.029	14 27 02.00	+33 00 48.9	0.89	0.82	17.448	15.461	48.4	0.787	0.697	0.3	26.6
ELAISR20 J142701+330525	19.359	0.020	19.645	0.020	14 27 01.63	+33 05 25.1	0.49	0.35	14.514	13.634	−0.6	0.015	0.014	0.0	23.5
ELAISR20 J142701+331222A	3.712	0.018	4.667	0.023	14 27 02.12	+33 12 27.7	0.49	0.36	16.831	14.568	−4.0	0.082	0.071	0.0	19.9
ELAISR20 J142701+331222B	2.324	0.018	2.858	0.022	14 27 01.52	+33 12 13.1	0.50	0.37	15.773	15.202	86.1	0.124	0.119	0.2	20.1
ELAISR20 J142701+331222T	3.712	0.025	7.433	0.031	14 27 01.89	+33 12 22.1	0.49	0.35	-	-	-	-	-	-	20.0

Note: The full catalogue is available from http://www.ast.cam.ac.uk/elais/

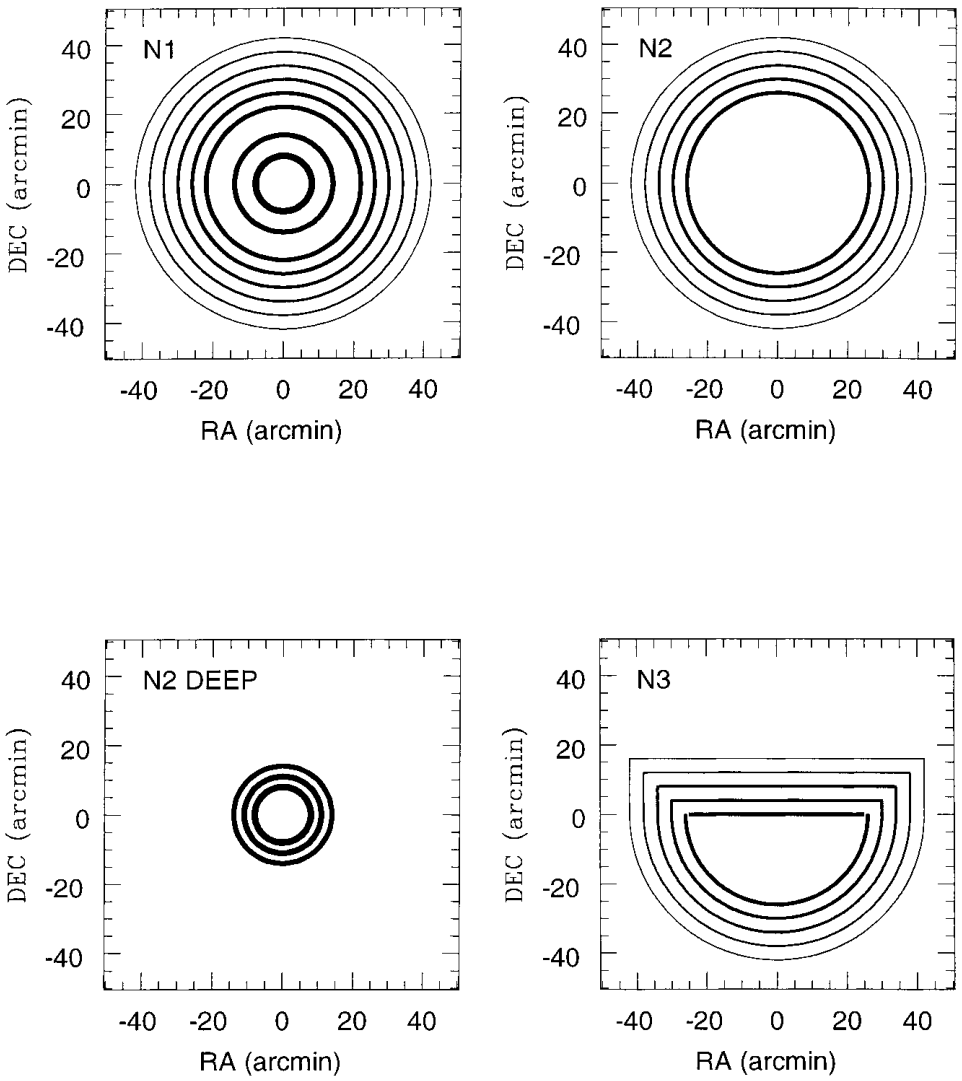

Figure 5. The region used for the source extraction. Lines with the same thickness enclose regions with the same rms noise value (see Table 2).

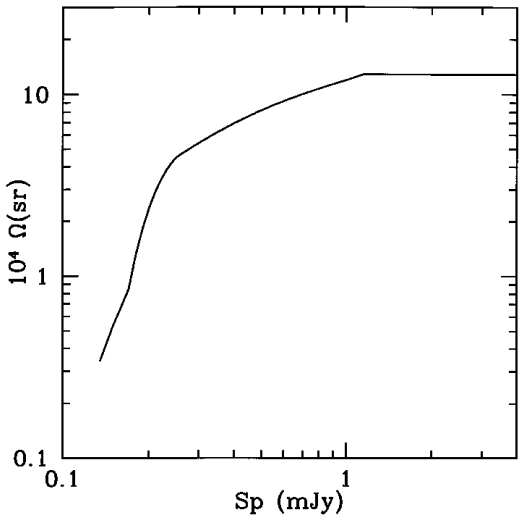

Figure 6. Solid angle over which a source with detected peak flux density S_P can be counted.

Using the data reported in Table 2 we obtained the solid angle $\Omega(S_P)$ as a function of the peak flux density S_P covered by our survey. This effective survey area is shown in Fig. 6.

4.2 Source detections

Within each region we searched for radio sources up to a peak flux density ≥ 5 times the rms value of the region. The sources were extracted using the task SAD (Search And Destroy), which attempts to find all the sources whose peaks are brighter than a given level. For each selected source the flux, the position and the size are estimated using a least-squares Gaussian fit. However, for faint sources a Gaussian fit may be unreliable [see Condon (1997) for an extensive discussion about errors in Gaussian fits]. For this reason we decided first to run the task SAD with a flux limit of three times the local rms value (see Table 2). Subsequently, we derived the peak flux of faint sources (those detected with $3\sigma < S_P < 7\sigma$) using a second-degree interpolation (task MAXFIT). Only the sources with a MAXFIT peak flux density $\geq 5\sigma$ were included in the sample. For these faint sources the total flux density was obtained using the task IMEAN, which integrates the map value in a specific rectangle, while for all the other parameters (major axis, minor axis and position

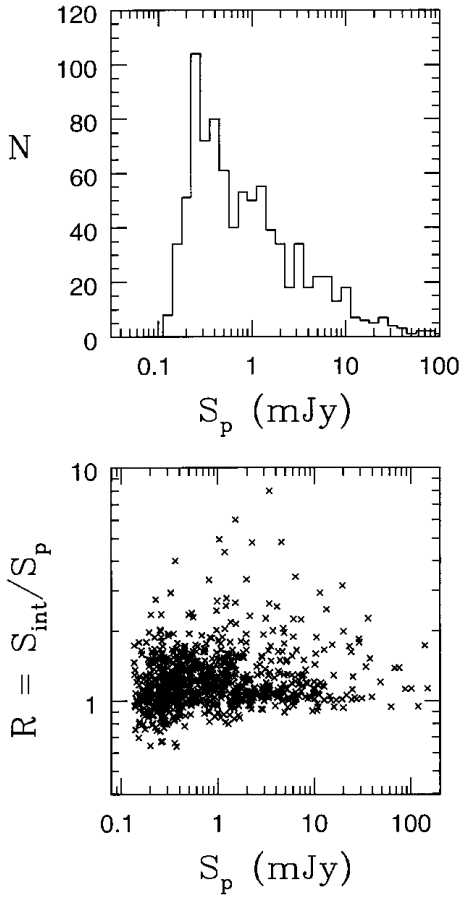

Figure 7. Peak flux distributions (upper panel) and total to peak flux ratio as a function of peak flux (lower panel) for all the radio sources detected in N1, N2 and N3.

Table 4. The number of radio sources detected in each field.

Field	Single sources	Multiple sources	Total sources
N1	345	16	361
N2	305	16	321
N3	173	12	185

angle) we used the values obtained with the Gaussian fit. For irregular resolved sources the total flux density was calculated using the task TVSTAT which allows use of an irregular area to integrate the map value.

4.3 Multiple sources

Detected sources separated by less than twice the value of our synthesized beam size (i.e., 30 arcsec) and with a flux ratio lower than 2 have been considered as a single source. We adopted this criterion because the component flux density ratio of real doubles is usually small ($\lesssim$2) while projection pairs can have arbitrarily large flux density ratios (Condon, Condon and Hazard 1982).

5 THE SOURCE CATALOGUE

Considering all the available observations we detected a total of 867 sources at $\geq 5\sigma$ level (44 of which have multiple components as defined in Section 4.3) over a total area of 4.222 deg^2. The catalogue with all the 867 sources (921 components) reports the name of the source, the peak flux density $S_{\rm P}$ in mJy, the total integrated flux density $S_{\rm I}$ in mJy, the RA and Dec. (J2000), the full width at half-maximum (FWHM) of the non-deconvolved major and minor axes $\theta_{\rm M}$ and $\theta_{\rm m}$ (in arcsec), the position angle PA of the major axis (in degrees measured east to north) and the off-axis angle in the VLA map (in arcmin). The different components of multiple sources are labelled 'A', 'B', etc., followed by a line labelled 'T' in which flux and position for the total sources are given. For these total sources the positions have been computed as the flux-weighted average position for all the components. Table 3 shows the first page of the catalogue as an example. The full catalogue is available from http://www.ast.cam.ac.uk/elais/.

In Table 4 we report the number of radio sources detected in N1, N2 and N3, while in Fig. 7 we show the distribution of the peak flux density and the total to peak flux ratio as a function of peak flux for all the 867 sources. Contour maps of all the 44 double or multiple sources are shown in Figs 8, 9 and 10.

5.1 Source parameters and their uncertainties

5.1.1 Positions and angular sizes

Following Condon (1997), the errors on the source parameters reported in the catalogue have been calculated using

$$\frac{\sigma^2_{S_{\rm P}}}{S^2_{\rm P}} = \frac{\sigma^2_{S_{\rm I}}}{S^2_{\rm I}} = \frac{\sigma^2_{\theta_{\rm M}}}{\theta^2_{\rm M}} = \frac{\sigma^2_{\theta_{\rm m}}}{\theta^2_{\rm m}} = \frac{\sigma^2_{\rm PA}}{2}\left(\frac{\theta^2_{\rm M}-\theta^2_{\rm m}}{\theta^2_{\rm M}\theta^2_{\rm m}}\right)^2 = \frac{2}{\rho^2}, \quad (1)$$

where ρ is the signal-to-noise ratio given by

$$\rho^2 = \frac{\pi}{8\ln 2}\frac{\theta_{\rm M}\theta_{\rm m}S^2_{\rm P}}{h^2\sigma^2_{\rm map}}. \quad (2)$$

Equations (1) and (2) are the master equations for estimating the variances of the parameters derived from a two-dimensional Gaussian fit on an image with a noise variance $\sigma^2_{\rm map}$ and pixel size h. In our maps $h = 3$ arcsec, while column 5 of Table 2 reports the value of $\sigma_{\rm map}$ as a function of the off-axis angle. The rms position errors are given by (Condon et al. 1998):

$$\sigma^2_\alpha = \varepsilon^2_\alpha + \sigma^2_{\theta_{\rm M}}\sin^2({\rm PA}) + \sigma^2_{\theta_{\rm m}}\cos^2({\rm PA}), \quad (3)$$

$$\sigma^2_\delta = \varepsilon^2_\delta + \sigma^2_{\theta_{\rm M}}\cos^2({\rm PA}) + \sigma^2_{\theta_{\rm m}}\sin^2({\rm PA}). \quad (4)$$

The mean image offsets $\langle\Delta\alpha\rangle$ and $\langle\Delta\delta\rangle$ and rms calibration uncertainties ε^2_α and ε^2_δ are best determined by comparison with accurate positions of sources strong enough that the noise plus confusion terms are much smaller than the calibration terms. We used the 37 single compact sources stronger than 10 mJy found in the FIRST (Faint Images of the Radio Sky at Twenty centimetres) radio survey (Becker, White and Helfand 1995). Their offsets $\langle\Delta\alpha\rangle$ and $\langle\Delta\delta\rangle$ are shown in Fig. 11. The mean offsets of our map are $\langle\Delta\alpha\rangle = -0.15 \pm 0.08$ arcsec and $\langle\Delta\delta\rangle = 0.18 \pm 0.06$ arcsec. The source coordinates reported in the catalogue (see Table 3) have been corrected for these offsets.

From the distribution of $\langle\Delta\alpha\rangle$ and $\langle\Delta\delta\rangle$ shown in Fig.11 we have

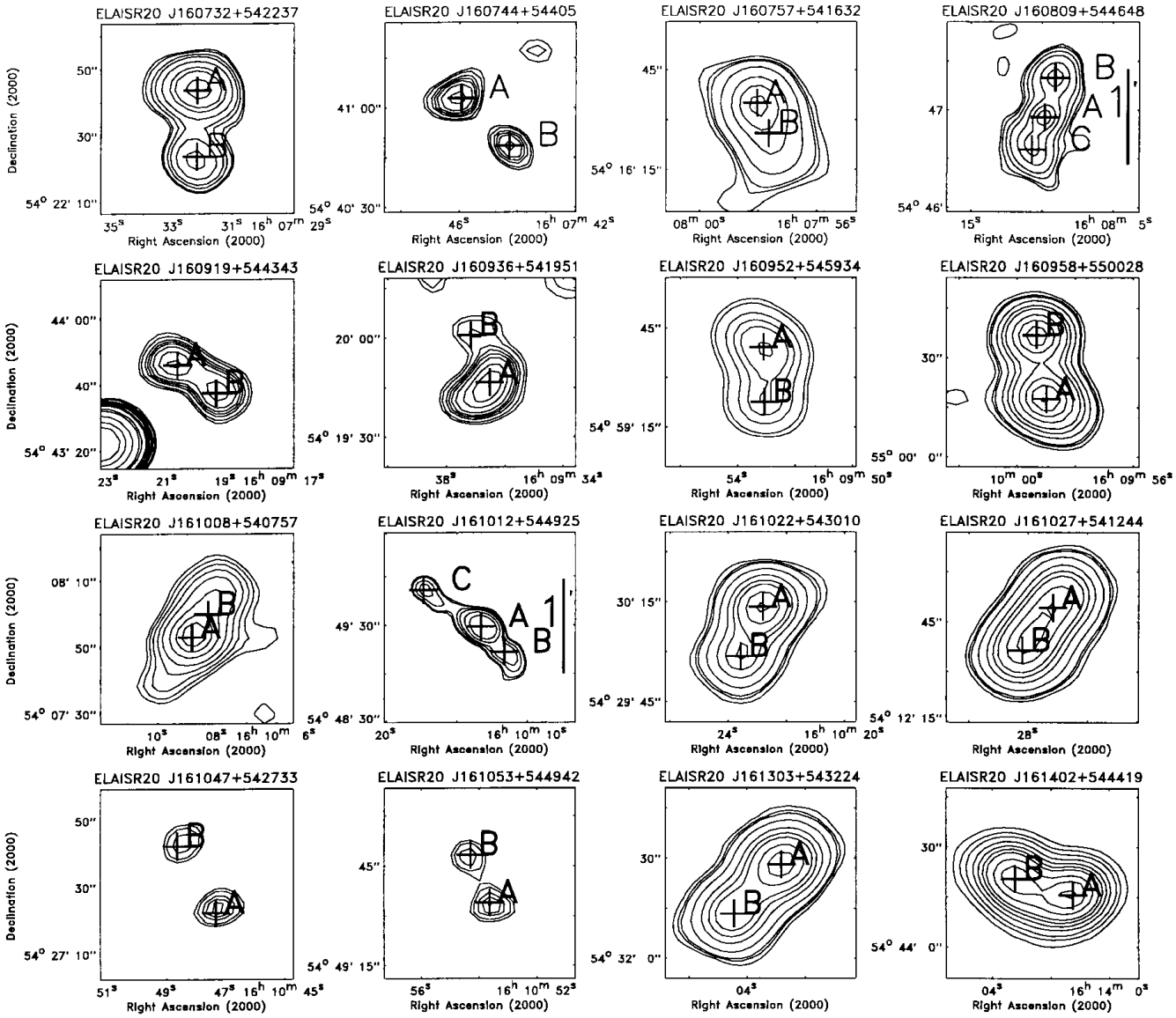

Figure 8. Contour maps for multiple sources in N1. Contour levels are 5, 6, 7, 8, 10,... times the local rms noise value (see Table 2). Each map is 1×1 arcmin^2 except for very extended sources for which the map size is variable. For these sources the vertical bar in the map shows 1 arcmin.

estimated the rms calibration errors: $\varepsilon_\alpha = 0.486$ arcsec and $\varepsilon_\delta = 0.351$ arcsec. Their small values show that our mosaic maps are not affected by relevant geometric distortions resulting from the approximation of a finite portion of the spherical sky away from the instrumental zenith with a bi-dimensional plane (see Perley 1989; Condon et al. 1998). Using the mean offsets and calibration errors obtained using the 37 sources stronger than 10 mJy in common with the FIRST survey, we have calculated the positional errors of all our sources. To verify that our positional errors are realistic also for faint sources, we used the 211 single compact sources stronger than 1 mJy found to be in common with the FIRST survey. The right ascension and declination differences $\langle \Delta\alpha \rangle$ and $\langle \Delta\delta \rangle$ were divided by the uncertainties σ_α and σ_δ (from equations 3 and 4). As expected, the normalized error distributions (Fig. 12) are Gaussian with nearly zero mean and unit variance, verifying that our positional uncertainties are accurate also for sources down to $\sim$1 mJy.

However, as shown in the flux distribution of Fig. 7, the majority of our radio sources have a flux lower than 1 mJy. Since we do not have other radio catalogues below 1 mJy to repeat our test, we decided to use our observations to test the reliability of the position errors down to the flux limit of our survey ($\sim$0.135 mJy). In particular, we used the following procedure. Each mosaic map has been obtained by combining five or more individual pointings, whose centres are separated by $\sim$22 arcmin. Because in each individual map the FWHM of the primary beam is 31 arcmin, there are many overlapping regions where sources are detected in two different pointings. We considered the sources detected in each individual pointing as an independent data set and used the sources in common (i.e. the sources detected in the overlapping regions) to test the reliability of the positional errors. We have a total of 134 sources in the overlapping regions with a flux density lower than 1 mJy. The right ascension and declination differences of these 134 sources were divided by the combined errors $\sigma_{\rm RA}$ and $\sigma_{\rm DEC}$, where

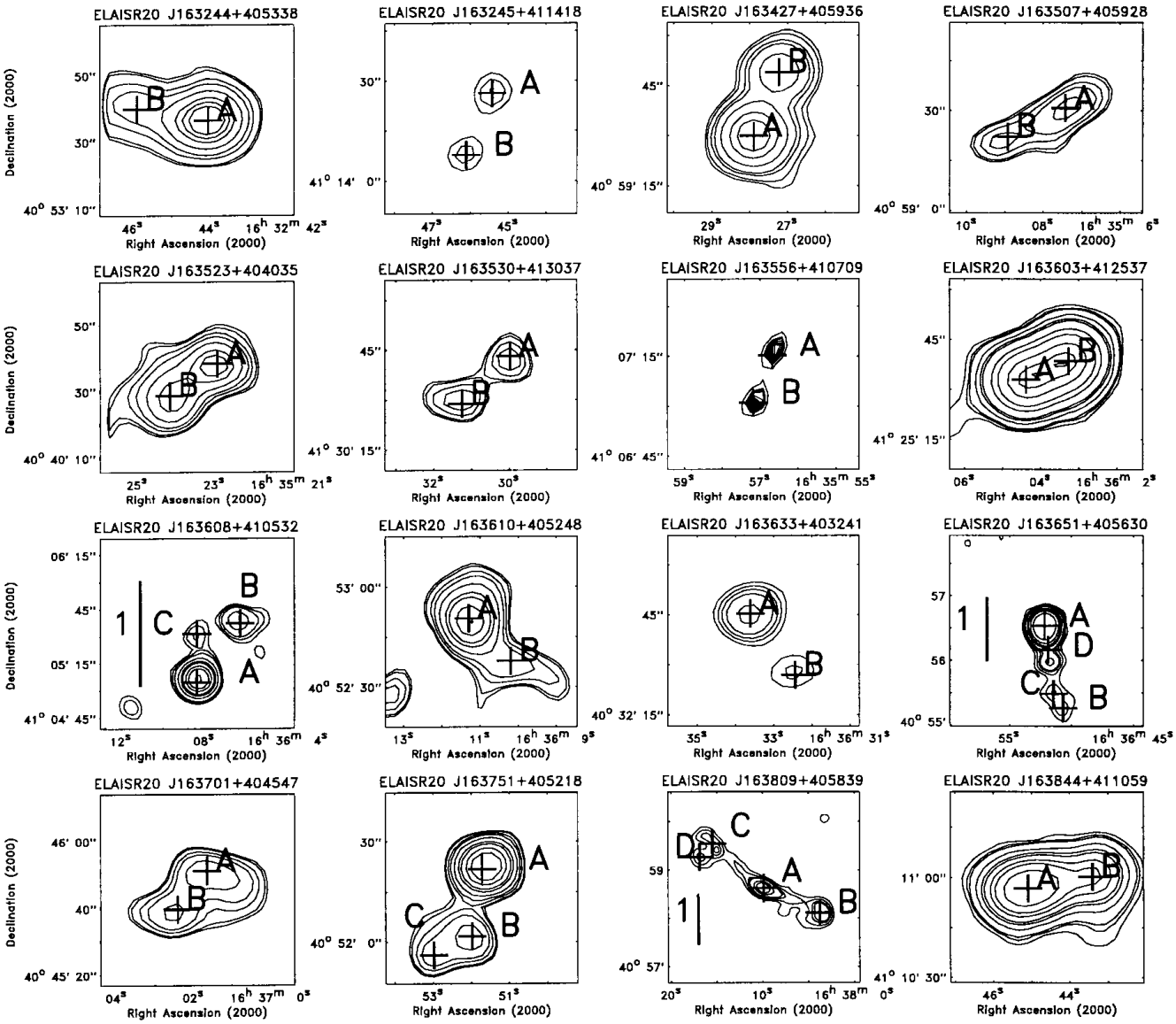

Figure 9. As in Fig. 8 for N2.

$\sigma^2_{\rm RA} = \sigma^2_{\alpha 1} + \sigma^2_{\alpha 2}$ and $\sigma^2_{\rm DEC} = \sigma^2_{\delta 1} + \sigma^2_{\delta 2}$ with $\sigma_{\alpha 1}, \sigma_{\alpha 2}, \sigma_{\delta 1}$ and $\sigma_{\delta 2}$ from equations (3) and (4). As shown in Fig. 13, these error distributions for faint sources also agree with the expected Gaussians (smoothed curves).

In conclusion the positional uncertainties obtained using equations (3) and (4) are accurate also for sources down to the limit of our survey (∼0.135 mJy) and they can be used to estimate the reliability of the optical and infrared identifications. The rms position uncertainties σ_α and σ_δ are plotted as functions of the flux density in Fig. 14. Typical values are ∼2 arcsec for the fainter sources (∼0.13 mJy) and ∼0.6 arcsec for the brighter sources (>10 mJy).

5.1.2 *Bandwidth smearing*

The principles upon which synthesis imaging is based are strictly valid only for monochromatic radiation. When radiation with a finite bandwidth is accepted, aberrations, or so-called bandwidth smearing, in the image will result. These take the form of radial smearing, which worsens with increasing distance from the centre. The peak response to a point source simultaneously declines in a way that keeps the integrated flux constant. In other words the bandwidth smearing reduces the peak flux density $S_{\rm P}$ of a source but not its integrated flux density $S_{\rm I}$. However, in our case, since we used spectral line mode where the bandwidth is narrower than in continuum mode, the bandwidth smearing should be negligible. To verify that this is the case, a strong calibrator (the source 3C 286) was observed at position offsets of 5, 10, 15, 20, 25, 30, 35 arcmin in two orthogonal directions (north–south and east–west) and we made a Gaussian fit of the source in each of the offset positions. The ratio between peak and total flux density ($S_{\rm P}/S_{\rm I}$) as a function of the off-axis angle is shown in Fig. 15; the bandwidth smearing is negligible up to $r \simeq 30$ arcmin from the centre of each single pointing. Therefore the resulting mosaic maps, where the distance between the single pointings is ∼22 arcmin, are not affected by relevant bandwidth smearing and point sources should have $S_{\rm P}/S_{\rm I} > 0.98$ everywhere.

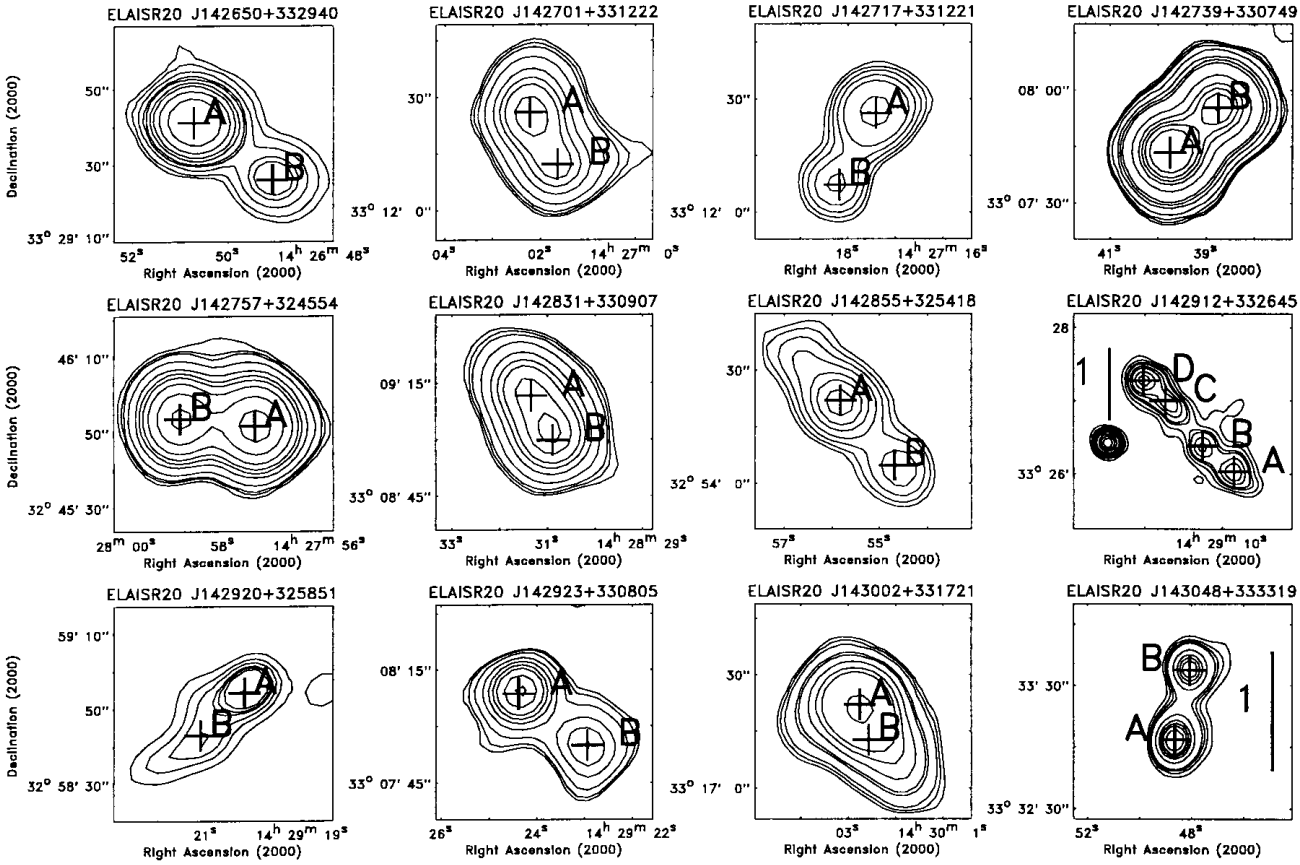

Figure 10. As in Fig. 8 for N3.

6 THE SOURCE COUNTS

The complete sample of 867 sources with $S_P > 5\sigma$ was used for the construction of the source counts. Sources with multiple components are treated as single radio sources. For all the sources we have used the total flux in computing the source counts. Every source was weighted for the reciprocal of its visibility area, $\Omega(S_P)^{-1}$ (see Figure 6), which is the area over which the source could have been seen above the adopted limit. The 1.4-GHz source counts of our survey are summarized in Table 5. For each flux density bin, the average flux density in each interval, the observed number of sources in each flux density interval, the differential source density (in sr^{-1} Jy^{-1}), the normalized differential counts $nS^{2.5}$ (in sr^{-1} $Jy^{1.5}$) with estimated errors (as $n^{1/2}S^{2.5}$) and the integral counts (in sr^{-1}) are given. The normalized 1.4-GHz counts are plotted in Fig. 16 where, for comparison, the differential source counts obtained with other 1.4-GHz radio surveys are also plotted, while the integral source counts (deg^{-2}) are plotted in Fig. 17. The solid line in Fig. 16 represents the global fit to the counts obtained by Windhorst et al. (1990) by fitting the counts from 24 different 1.4-GHz surveys. The open circles represent the counts obtained using the 1.4-GHz survey FIRST (White et al. 1997). Finally, the open stars represent the 1.4-GHz counts obtained by Gruppioni et al. (1997) in a recent radio survey in the Marano Field (RA = 03^h 15^m, Dec. = $-55°$ $13'$).

As shown in the figure, there is a very good agreement between our counts and those obtained with other surveys. In particular, the points at the fainter flux level confirm the well-known flattening observed in the normalized differential source counts below a few mJy (Windhorst et al. 1990). The roll-off of the sources in the FIRST survey (open circles in Fig. 16) at flux densities less than ~2 mJy arises because of the low peak flux densities of many faint, extended sources, which make them undetectable in the FIRST survey. As noted by White et al. (1997) this is a clear indication of the incompleteness of the FIRST survey at the faint limit. On the other hand, the very good agreement between our counts and those obtained with other surveys (also at very faint flux levels) and the lack of any roll-off at faint flux levels in our counts indicate that our procedure for the source extraction (see above) yields very good results and that our sample is not affected by incompleteness at the faint limit.

A maximum-likelihood fit to our 1.4-GHz counts with two power laws:

$$\frac{dN}{dS} \propto \begin{cases} S^{-\alpha_1} & \text{if } S > S_b \\ S^{-\alpha_2} & \text{if } S < S_b \end{cases} \quad (5)$$

gives the following best-fitting parameters: $\alpha_1 = 1.71 \pm 0.10$, $\alpha_2 = 2.36 \pm 0.20$, $S_b \simeq 0.5$ mJy. These values suggest that the re-steepening of the integral counts towards a Euclidean slope starts below 1 mJy, in agreement with Gruppioni et al. (1997), Condon & Mitchell (1984) and Windhorst, van Heerde & Katgert (1984), while Windhorst et al. (1990), by fitting the counts of several 1.4-GHz surveys, found that the change in slope starts around 5 mJy.

7 COMPARISON WITH THE NVSS AND FIRST RADIO CATALOGUES

The regions that we are observing with the VLA are also covered by

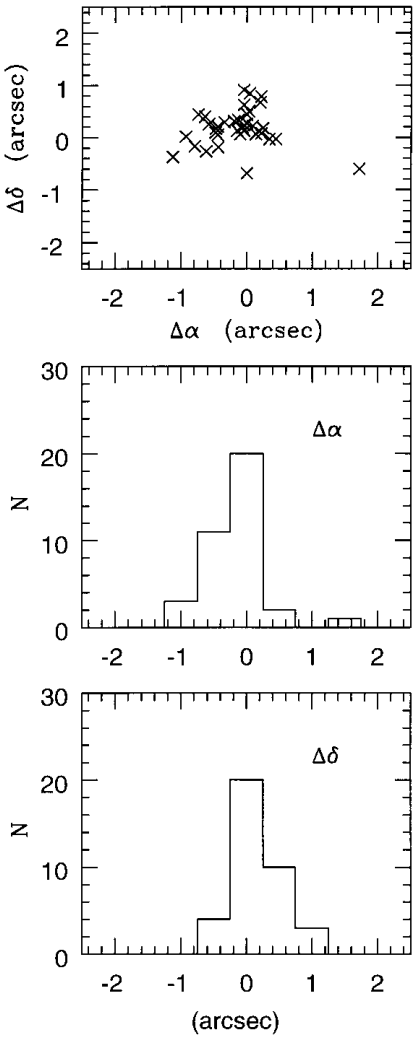

Figure 11. Position errors for strong point sources (37 sources in our survey and in the FIRST survey with radio flux greater than 10 mJy).

the NVSS (Condon et al. 1998) and FIRST (Becker et al. 1985; White et al. 1997) radio surveys. The NVSS (NRAO VLA Sky Survey) covers the sky north of J2000 $\delta = -40°$ at 1.4 GHz with $\theta = 45$ arcsec resolution and a nearly uniform sensitivity of 0.45 mJy (1σ), while the FIRST (Faint Images of the Radio Sky at Twenty centimetres) will cover over 10 000 deg^2 at 1.4 GHz with a typical 1σ rms of 0.15 mJy and a resolution of 5.4 arcsec.

It was therefore natural to make a comparison between our results and the results obtained by the NVSS and FIRST surveys on the same regions of the sky. In Section 7.1 we discuss the reliability of the software that we are using to extract the radio sources (SAD in the AIPS version 1996 October), while in Section 7.2 we report the comparison between our VLA observations and the NVSS and FIRST source catalogues.

7.1 SAD on the NVSS and FIRST maps

As a first step we used the NVSS and FIRST radio maps and the published catalogues to test the reliability of the software that we are using to extract radio sources. From the NVSS and FIRST archives, we retrieved the maps covering the region of the sky N2 (see Table 1).

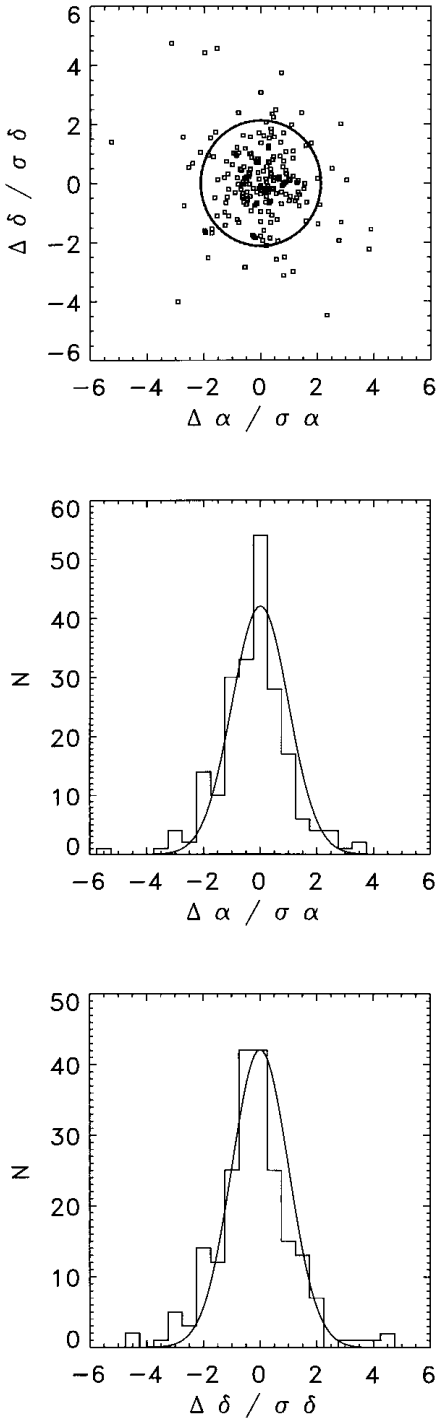

Figure 12. Position errors for the 211 point sources stronger than 1 mJy in common with the FIRST survey, in units of the calculated position uncertainties σ_α and σ_δ, along with the 90 per cent confidence error circle (upper panel). The smooth curves in the central and lower panels represent the expected Gaussian of zero mean and unit variance.

From the NVSS archive we retrieved the map I1640P40 while from the FIRST archive we retrieved the maps F16330+40417, F16330+41132, F16360+40417, F16360+41132, F16390+40417 and F16390+41132.

Using the AIPS software SAD on these maps, we obtained two lists of sources (one for the NVSS and one for the FIRST) in the same

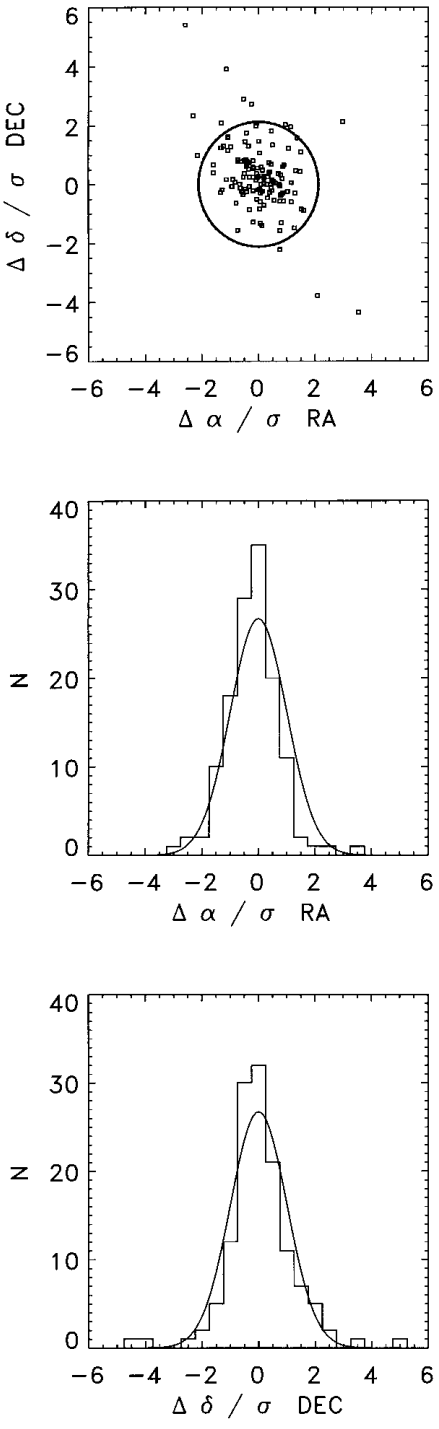

Figure 13. Position errors for the 134 point sources in the overlapping region with flux lower than 1 mJy, in units of the combined position uncertainties σ_{RA} and σ_{DEC}, along with the 90 per cent confidence error circle (upper panel). The smooth curves in the central and lower panels represent the expected Gaussian of zero mean and unit variance.

region covered by our VLA observations. These two lists were compared with the list of sources obtained from the NVSS and FIRST catalogues in which are reported the sources above the 5σ limits of each survey. The results are reported in Table 6 and in Fig. 18.

All three NVSS sources missing in the list obtained by us using

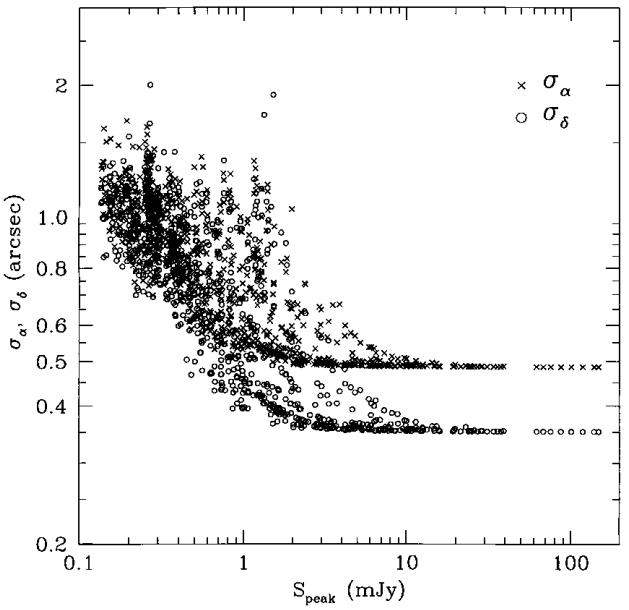

Figure 14. The typical rms position uncertainties σ_α and σ_δ for point sources of flux density S_P.

SAD on the NVSS map are present in our deeper VLA map. Therefore they are real sources not detected by SAD. Their flux densities are lower than 3 mJy, close to the 5σ limit of the NVSS map.

Three (FIRST 163637.9+410511, 163707.5+405125 and 163815.4+405840) of the eight sources present in the FIRST catalogue but not detected by us using SAD on the FIRST map are also not detected in our deeper VLA maps to a flux limit of 0.1 mJy, so they are spurious sources. The other five sources missing in the FIRST list (as well as the four sources detected by SAD but not in the FIRST catalogue) have a peak flux density $\lesssim$1.2 mJy, i.e. very

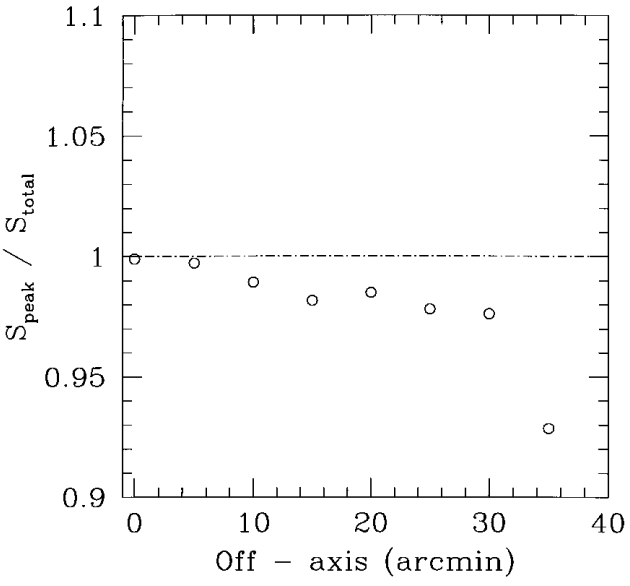

Figure 15. Bandwidth smearing reduces the peak flux density S_P of a point source but preserves the integrated flux density S_I. Abscissa: angular distance from the centre (arcmin). Ordinate: the observed ratio S_P/S_I.

Table 5. The 1.4-GHz radio source counts.

S (mJy)	$\langle S \rangle$ (mJy)	N_S	dN/dS (sr^{-1} Jy^{-1})	$nS^{2.5}$ (sr^{-1} Jy$^{1.5}$)	$N(>S)$ (sr^{-1})
0.13–0.23	0.17	87	8.962×10^9	3.60 ± 0.39	2.001×10^6
0.23–0.42	0.32	188	2.641×10^9	4.61 ± 0.34	1.076×10^6
0.42–0.76	0.56	148	6.301×10^8	4.78 ± 0.39	5.814×10^5
0.76–1.36	1.02	127	1.990×10^8	6.56 ± 0.58	3.691×10^5
1.36–2.46	1.83	112	8.139×10^7	11.68 ± 1.10	2.485×10^5
2.46–4.42	3.30	64	2.543×10^7	15.86 ± 1.98	1.597×10^5
4.42–7.96	5.93	53	1.166×10^7	31.61 ± 4.34	1.097×10^5
7.96–14.33	10.68	43	5.251×10^6	61.87 ± 9.43	6.842×10^4
14.33–25.79	19.22	17	1.153×10^6	59.07 ± 14.33	3.499×10^4
25.79–46.41	34.60	13	4.900×10^5	109.10 ± 30.25	2.177×10^4
46.42–83.55	62.27	8	1.675×10^5	162.10 ± 57.31	1.166×10^4
83.55–150.39	112.09	5	5.816×10^4	244.70 ± 109.40	5.443×10^3
150.39–270.70	201.77	2	1.293×10^4	236.40 ± 167.10	1.555×10^3

close to the FIRST flux limit. These differences are probably the result of the unreliable Gaussian fit of faint sources as discussed above. Moreover we have to consider that the source lists (our SAD list and the catalogue lists) are obtained using different source extraction software. In fact, both NVSS and FIRST sources are extracted with special AIPS-based routines written exclusively for each survey (see Condon et al. 1993 and White et al. 1997 for more details).

Therefore, in conclusion, we are confident in using SAD as source extraction software, keeping in mind that for faint sources the flux obtained with a Gaussian fit may be unreliable.

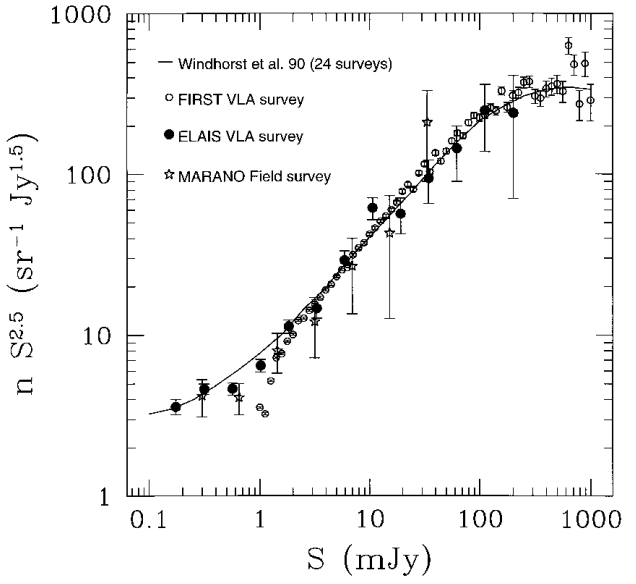

Figure 16. The normalized differential source counts. The abscissa gives the flux density (mJy) and the ordinate gives the differential number of sources normalized by $S^{2.5}$ (sr^{-1} Jy$^{+1.5}$). The solid line represents the global fit to the counts obtained by Windhorst et al. (1990) by fitting the counts from 24 different 1.4-GHz surveys. The open circles represent the counts obtained using the 1.4-GHz survey FIRST (White et al. 1997), the filled circles are the counts obtained using our VLA observations in the ELAIS regions and the open stars represent the 1.4-GHz counts obtained by Gruppioni et al. (1997) in the Marano Field.

7.2 Comparison between our VLA observations and the NVSS and FIRST source catalogues

The primary difficulty in comparing the three surveys is the difference in angular resolution. A summary of the main properties of the NVSS, FIRST and our VLA survey is reported in Table 7.

The high-resolution surveys will partially resolve extended sources that appear point-like in the low-resolution surveys, so that the flux density of the sources will be smaller in FIRST and our survey than in the NVSS. To minimize this problem, we restricted the comparison to compact sources (i.e. sources with $S_I/S_P < 2$) with an off-axis angle in our VLA map less than 34 arcmin. The restriction on the off-axis angle allows us to use only the sources detected in regions where the 5σ limit is well below the limit of the FIRST survey (see Tables 2 and 7). For the NVSS and FIRST surveys we used the public source catalogues as available on 1998 February 1.

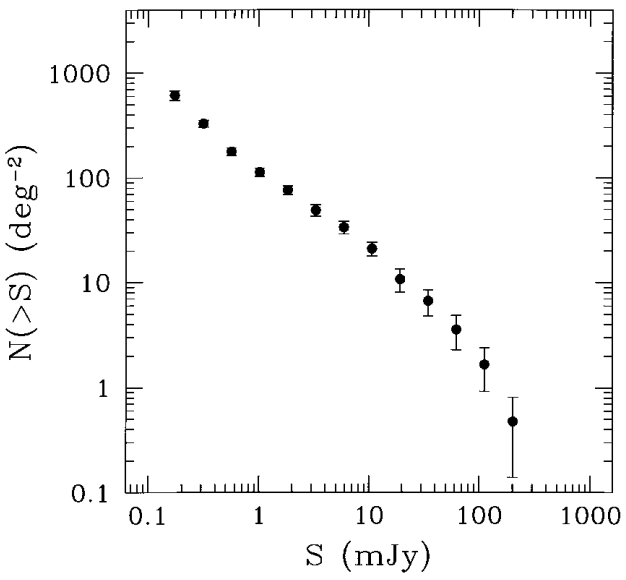

Figure 17. The integral source counts. The abscissa gives the flux density (mJy) and the ordinate gives the total number of sources per square degree.

Table 6. Comparison between SAD and NVSS – FIRST catalogues.

Survey	Published catalogue sources	Sources in our SAD list	Common sources	Published catalogue sources not in our SAD list	Our SAD sources not in the published catalogue
NVSS	46	43	43	3	0
FIRST	74	70	66	8	4

Table 7. Comparison of NVSS, FIRST and our VLA survey.

	NVSS	FIRST	Our VLA data
VLA configuration	D	B	C
Beam size	45 arcsec	5 arcsec	15 arcsec
Confusion noise	0.08 mJy	0.002 mJy	0.011 mJy
Exposure time	30–60 s	3 min	~1 h
1σ rms noise	0.45 mJy	0.15 mJy	0.05 mJy
5σ rms limit	2.25 mJy	0.75 mJy	0.25 mJy

Note: The rms confusion from faint extragalactic source in C configuration at 20 cm is 0.01 mJy (Mitchell & Condon 1985). The value for D configuration comes from Condon et al. (1998).

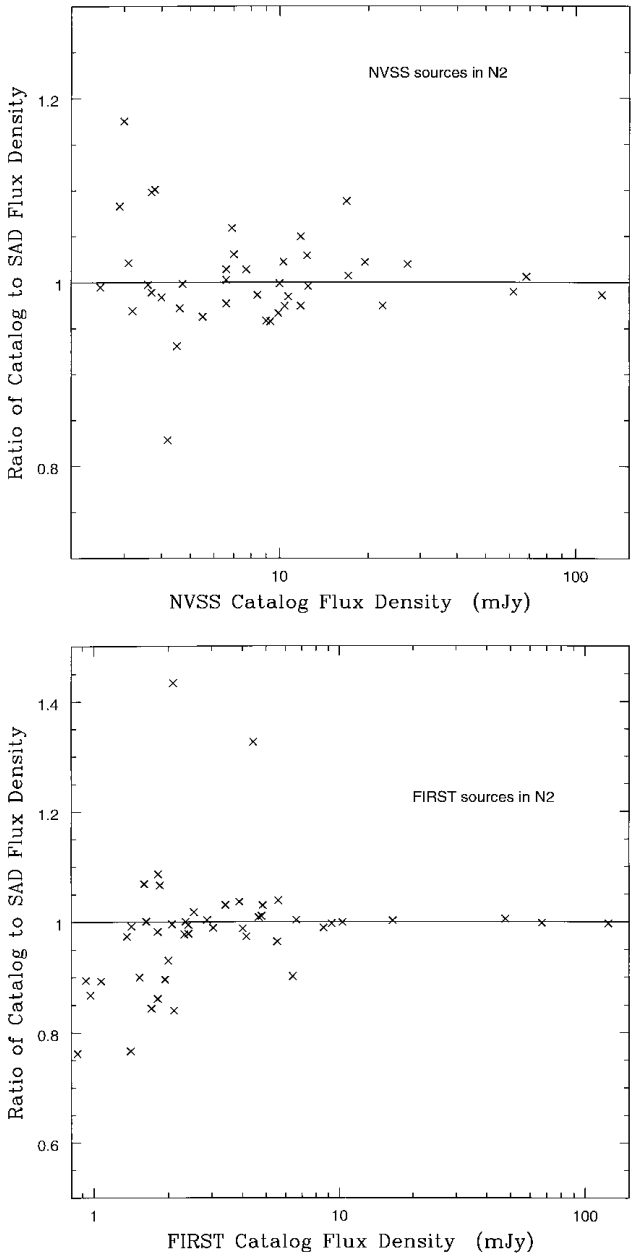

Figure 18. Ratio of flux reported in the public catalogue to our flux obtained using SAD on the respective radio maps as a function of the flux reported in the catalogue for the NVSS (top panel) and for the FIRST (lower panel) surveys.

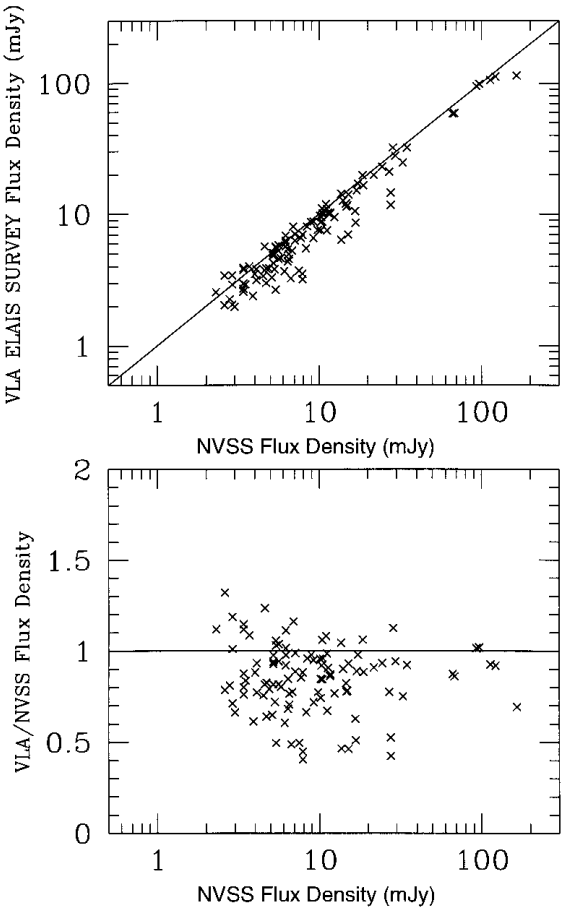

Figure 19. The peak flux obtained with our VLA survey versus the NVSS peak flux density as reported in the public catalogue (upper panel) and the ratio of our VLA to NVSS peak flux density as a function of the NVSS flux density (lower panel).

7.2.1 Our VLA survey versus the NVSS survey

Using the restriction of an off-axis value lower than 34 arcmin and a peak flux density $S_P > 2.3$ mJy ($\sim 5\sigma$ rms limit of the NVSS survey) we have 109 compact sources in common with the NVSS survey. In Fig. 19 we show a comparison between our VLA and NVSS total flux densities. A comparison between the flux density scales is discussed below. Besides these 109 common sources, there is one NVSS source (NVSS J142753+330837) that we did not detect in our survey plus five sources (with $S_P > 2.3$ mJy) detected in our maps but not in the NVSS survey. In Figs 20 and 21 we display a contour plot of these sources. For comparison, a contour plot of the FIRST image in the same region of the sky is also shown. As shown in Fig. 20 the NVSS source missing in our survey is also not detected in the FIRST survey. Its NVSS radio flux is 2.3 mJy, very close to the 5σ detection limit of the survey. It is probably a spurious NVSS source but it could also be a variable radio source. For the five sources missing in the NVSS survey, Fig. 21 clearly shows that one (ELAISR20 J142917+332626) is missing because our higher-resolution survey has resolved an extended NVSS source, one (ELAISR20 J142940+330552) is completely undetected on the NVSS map, and the other three sources are detected also in the NVSS map but below the 5σ limit (~ 2.25 mJy).

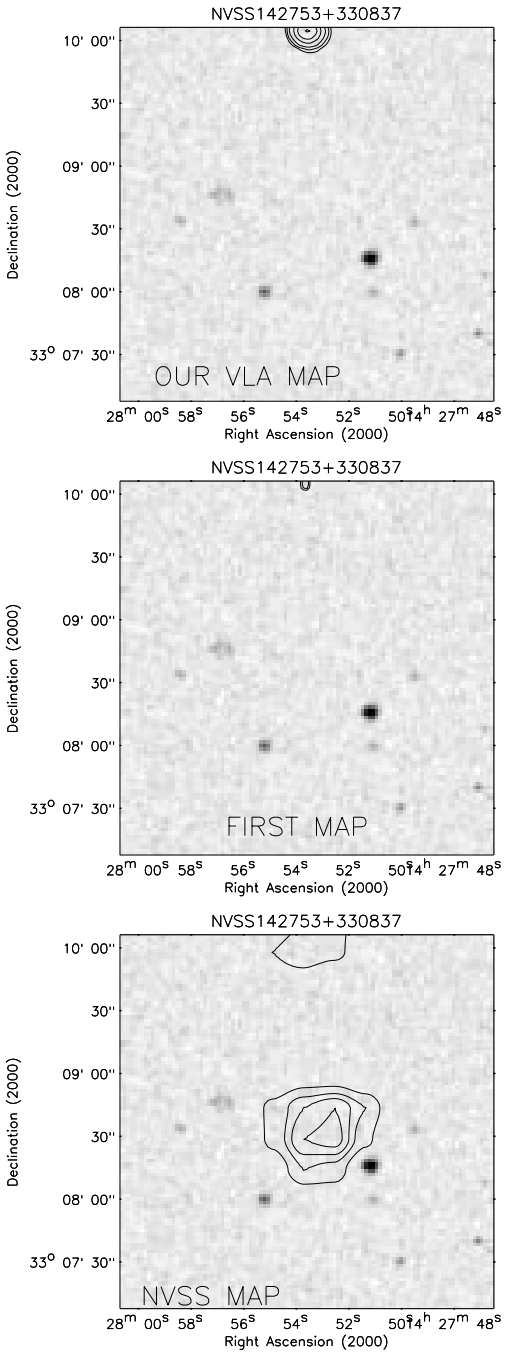

Figure 20. Radio contour plot of the NVSS source NVSS J142753+330837 present in the NVSS catalogue but not found either in our VLA map or in the FIRST catalogue, superimposed on the optical Digitized Sky Survey (DSS) image. All the maps have a size of 3×3 arcmin^2. Radio contour levels are 0.25, 0.35, 0.5, 0.75, 1.0, 1.5, 1.8, 2.5 mJy for our map, 0.75, 1.0, 1.5, 1.8, 2.5 mJy for the FIRST maps and 1.0, 1.3, 1.5, 1.7, 1.8, 2.0, 2.2, 2.5 mJy for the NVSS map.

All these five sources are present in the FIRST catalogue (and in the FIRST map as clearly shown in Fig. 21). Their absence in the NVSS catalogue is an indication of the incompleteness of the NVSS survey near that limit. A summary of the comparison between our survey and the NVSS and FIRST catalogue, the relative completeness and reliability is reported in Table 8 as a function of various flux density limits.

7.2.2 Our VLA survey versus the FIRST survey

Using the restriction of an off-axis value lower than 34 arcmin and a peak flux density $S_P > 1.0$ mJy (the limit of the FIRST catalogue), we have 216 compact sources in common with the FIRST survey. Six (FIRST J142953+330541, J143027+332249, J160636+543249, J160647+541511, J163607+410000 and J163730+405951) of these 216 common sources are flagged in the FIRST catalogue as a possible sidelobe of a nearby bright sources. In Fig. 22 we show a comparison between our VLA and FIRST total (integrated) flux densities.

Besides these 216 common sources, there are 14 FIRST sources (three of which are flagged: FIRST J163640+410016, J163646+405442 and J163654+404757) that we did not detect in our survey and 28 sources present in our survey but not in the FIRST catalogue. A flux distribution and contour maps of these last 28 sources are shown in Figs 23 and 24 respectively, while contour maps of the 14 FIRST sources that we did not detect are shown in Fig. 25. As shown in Fig. 23, all the radio sources missing in the FIRST catalogue have a peak flux density lower than 2 mJy. However, as shown in Fig. 24, many of them appear on the FIRST maps. This result confirms the incompleteness of the FIRST survey below ~ 2 mJy, as already indicated by the differential source counts reported in Fig. 5. On the other hand, Fig. 25 shows that many of the 14 FIRST sources missing in our survey probably are not real. Some of them may be uncleaned residual sidelobes around strong sources (see, for example, FIRST J161318+541607 and J163815+405840) or simply spurious sources in a not well cleaned map (see, for example, the FIRST maps of FIRST J161351+543258, J163634+413013 and J163706+405125). The completeness and reliability of the FIRST survey as a function of various flux limits are reported in Table 8.

7.2.3 Flux comparison between the three surveys

As shown in Figs 19 and 22 the flux densities of our survey are in good agreement with the FIRST and NVSS flux densities over two

orders of magnitude. However, as expected, the high-resolution surveys tend to estimate lower fluxes than the lower-resolution survey. This effect is evident in the lower panels of Figs 19 and 22: our VLA flux densities are, on average, lower than the NVSS flux densities but higher than the FIRST flux densities. High-resolution surveys, with their smaller synthesized beam size, lose flux as a result of the resolution surface brightness effect.

8 SUMMARY

Using the Very Large Array (VLA) radio telescope, we observed at 1.4 GHz a total area of 4.222 deg^2 in the *ISO*/ELAIS regions N1, N2 and N3. The lowest flux density reached by our observation is 0.135 mJy (at 5σ level) over an area of 0.118 deg^2, while the bulk of the observed regions are mapped with a flux density limit of 0.250 mJy (5σ). The data were analysed using the NRAO AIPS reduction package. The source extraction has been carried out with the AIPS task SAD. The reliability of SAD has been tested using the maps of the radio surveys FIRST and NVSS.

Considering all the available observations, we detected a total of 867 sources at 5σ, 44 of which have multiple components. These sources were used to calculate the normalized differential source counts. They provide a check on catalogue completeness and reliability plus information about source evolution. A comparison with other surveys shows very good agreement, confirming the presence of the well-known flattening of the counts below 1 mJy, the completeness of our catalogue, and the reliability of our procedure for source extraction.

A comparison with the FIRST and NVSS radio surveys quantifies the completeness of these two surveys near their flux density limits (5σ) of 1 and 2.3 mJy respectively. Considering the whole sample, we found a completeness of 96^{+2}_{-3} per cent for the NVSS and 89^{+2}_{-3} per cent for the FIRST survey. The probable cause of the lower completeness in the FIRST survey is the 'missing flux' caused by the higher spatial resolution as discussed by Becker et al. (1995) and White et al. (1997). Near their flux density limit the incompleteness reaches values of ~40 per cent for the NVSS and ~22 per cent for the FIRST survey, although these values are based on quite small numbers of sources. A flux comparison between the three surveys has shown that our survey with the VLA array in C configuration is a good compromise between high- and low-resolution radio surveys for our present purposes. The positional errors of the radio sources are ~2 arcsec for the fainter sources (~0.13 mJy) and ~0.6 arcsec for the brighter sources (>10 mJy). This small value will enable us to obtain reliable optical and far- infrared identification of the radio sources.

ACKNOWLEDGMENTS

This work was supported by the EC TMR Network programme (FMRX-CT96-0068). RGM thanks the Royal Society for support. We thank David Helfand for a careful reading of the manuscript, discussions and suggestions; Rick White for discussions on the optimal pointing grid; and both Bob Becker and Jim Condon for discussion on the optimal observing strategy; and Bob Becker for the provision of a FIRST observe file.

REFERENCES

Becker R. H., White R. L., Helfand D. J., 1995, ApJ, 450, 559
Benn C. R., Rowan-Robinson M., McMahon R. G., Broadhurst T. J., Lawrence A., 1993, MNRAS, 263, 98
Cesarsky C. et al., 1996, A&A, 315, L32
Condon J. J., 1997, PASP, 109, 166
Condon J. J., Mitchell K. J., 1984, AJ, 89, 610
Condon J. J., Condon M. A., Hazard C., 1982, AJ, 87, 739
Condon J. J., Anderson M. L., Helou G., 1991, ApJ, 376, 95
Condon J. J., Cotton W. D., Greisen E. W., Perley R. A., Yin Q. F., Broderick J. J., 1993, A&AS, 183, 640
Condon J. J., Cotton W. D., Greisen E. W., Yin Q. F., Perley R. A., Taylor G. B., Broderick J. J., 1998, AJ, 115, 1693
Fomalont E. B., Windhorst R. A., Kristian J. A., Kellerman K. I., 1991, AJ, 102, 1258
Gruppioni C., Zamorani G., de Ruiter H. R., Parma P., Mignoli M., Lari C., 1997, MNRAS, 286, 470
Helou G., Soifer B. T., Rowan-Robinson M., 1985, ApJ, 298, L7
Kessler M. F. et al., 1996, A&A, 315, L27
Lemke D. et al., 1994, in Klaas, U., Krger, H., Heinrichsen, I., Heske, A., Laureijs, R., eds, ISOPHOT Observer's Manual. ESA Publications Division, Noordwijk
Mitchell K. J., Condon J. J, 1985, AJ, 90, 1957
Oliver S. et al., 1997, in McLean B., ed., Proc. IAU Symp. 179, New Horizons from Multi-Wavelength Sky Surveys. Kluwer, Dordrecht, in press
Perley R. A., 1989, in Perley R. A., Schwab F. R., Bridle A. H., eds, Synthesis Imaging in Radio Astronomy. Astron. Soc. Pac., San Francisco, p. 259
Rowan-Robinson M. et al., 1991, Nat, 351, 719
Rowan-Robinson M., Benn C. R., Lawrence A., McMahon R. G., Broadhurst T. J., 1993, MNRAS, 263, 123
White R. L., Becker R. H., Helfand D. J., Gregg M. D, 1997, ApJ, 475, 479
Windhorst R. A., van Heerde G. M., Katgert P., 1984, A&AS, 58, 1
Windhorst R. A., Mathis D. F., Neuschaefer L. W., 1990, in Kron R. G., ed., ASP Conf. Ser. Vol. 10, Evolution of the Universe of Galaxies. Bookcrafters, Provo, p. 389
Wunderlich E., Klein U., Wielebinski R., 1987, A&AS, 69, 487

This paper has been typeset from a TEX/LATEX file prepared by the author.

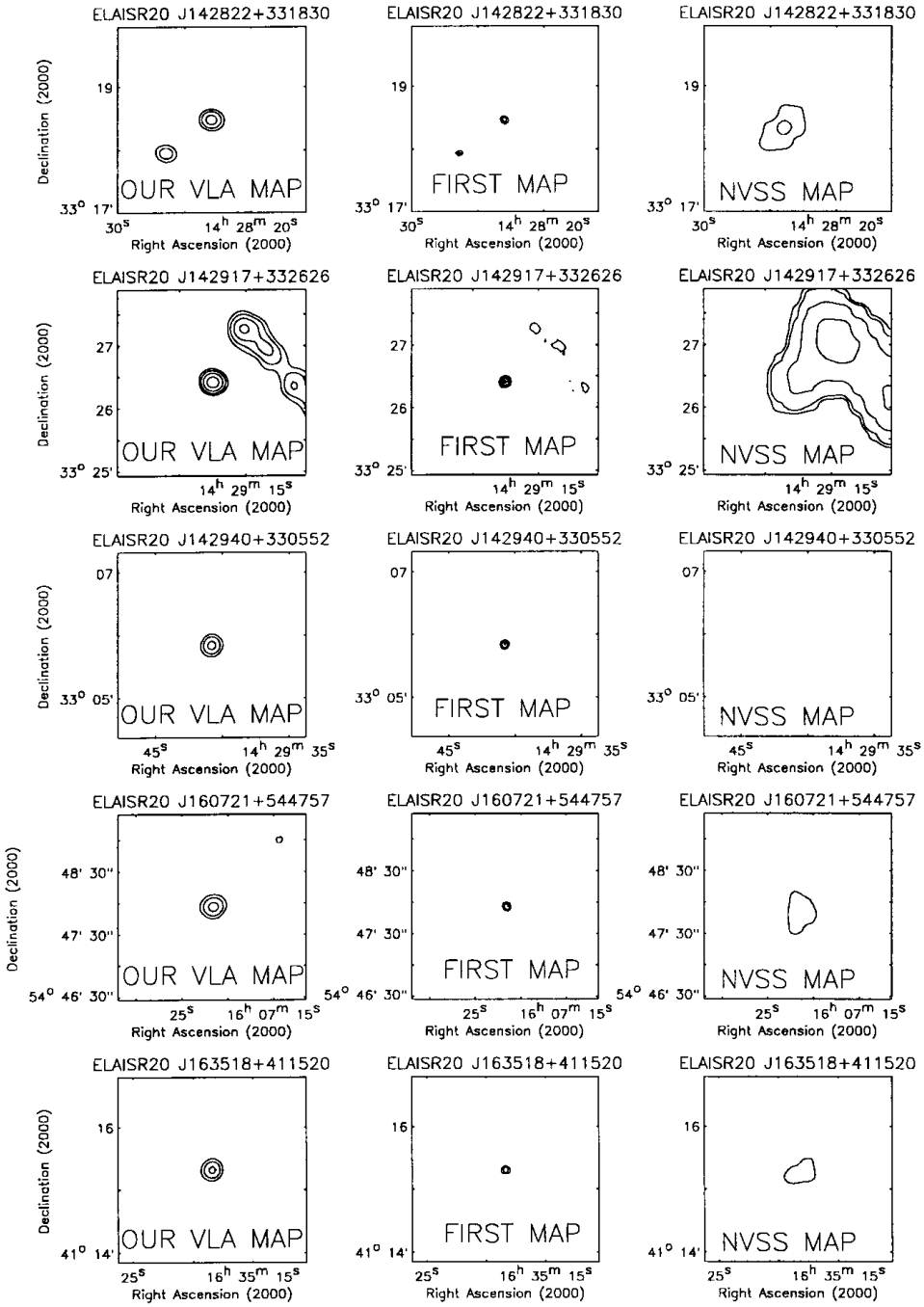

Figure 21. Contour plot of the five sources detected in our VLA and FIRST survey but not in the NVSS catalogue. All the maps have a size of 3×3 arcmin^2 . The contour levels are 0.5, 1, 2, 4, 8 mJy for our VLA maps and the FIRST maps and 1.5, 2, 4, 8 mJy for the NVSS maps.

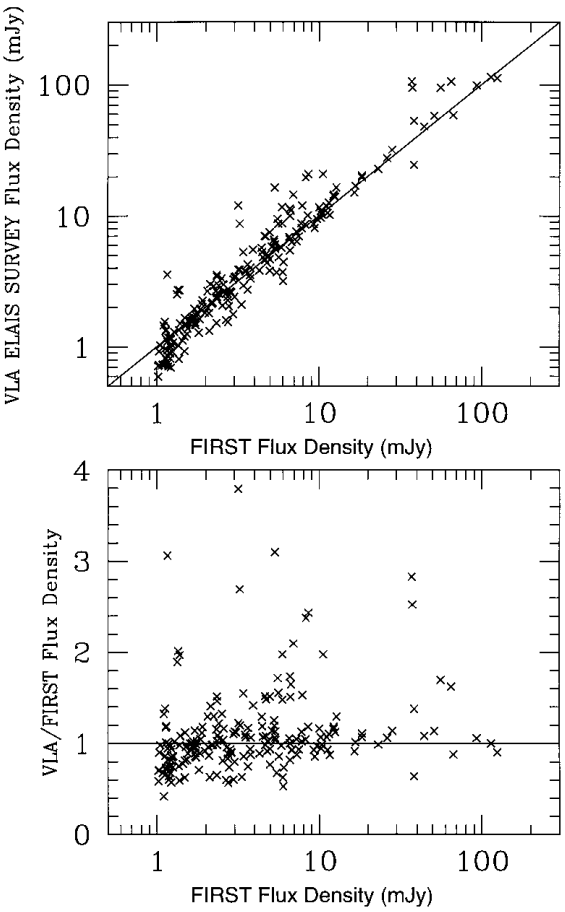

Figure 22. The flux density obtained with our VLA survey versus the FIRST flux density as reported in the public catalogue (upper panel) and the ratio of our VLA to FIRST flux density as a function of the FIRST flux density (lower panel). Because the FIRST integrated flux density is unreliable for flux density lower than 2 mJy (Helfand, private communication, see also Section 4.2) we used the peak flux densities for sources below 2 mJy and the integrated flux densities for sources above 2 mJy.

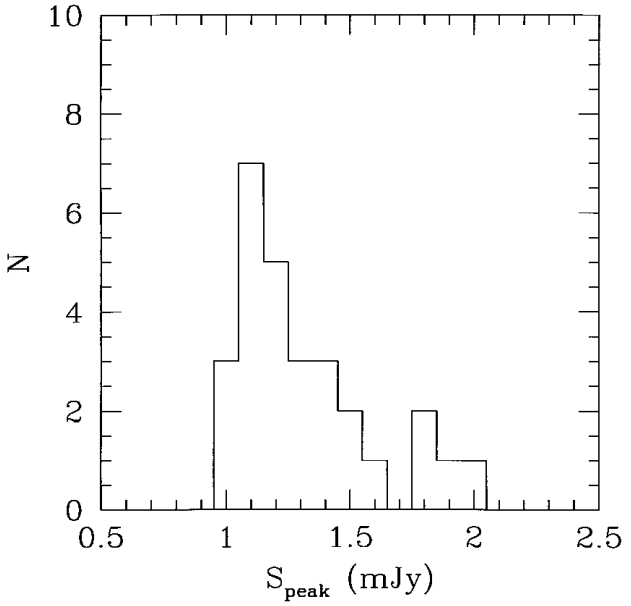

Figure 23. Flux density distribution of the 28 sources detected in our survey with a peak flux density $S_P > 1$ mJy but not present in the FIRST catalogue.

Table 8. Comparison between our VLA observations and NVSS – FIRST catalogues.

(a) NVSS					
Flux limit	Common sources	Sources detected in our survey not in the NVSS catalogue	Source in the NVSS catalogue not in our maps	Completeness of the NVSS survey (per cent)	Reliability of the NVSS sources (per cent)
$2.3 < S_{NVSS} < 3$ mJy	7	5	1	58^{+20}_{-21}	88^{+10}_{-20}
$3 < S_{NVSS} < 4$ mJy	9	–	–	100^{+0}_{-24}	100^{+0}_{-24}
$4 < S_{NVSS} < 5$ mJy	9	–	–	100^{+0}_{-24}	100^{+0}_{-24}
All sources	109	5	1	96^{+2}_{-3}	99^{+1}_{-2}
(b) FIRST					
Flux limit	Common sources	Sources detected in our survey not in the FIRST catalogue	Source in the FIRST catalogue not in our maps	Completeness of the FIRST survey (per cent)	Reliability of the FIRST sources (per cent)
$1 < S_{FIRST} < 2$ mJy	101 (6)	28	14 (3)	78^{+5}_{-5}	88^{+3}_{-4}
$2 < S_{FIRST} < 3$ mJy	34	–	–	100^{+0}_{-6}	100^{+0}_{-6}
$3 < S_{FIRST} < 4$ mJy	18	–	–	100^{+0}_{-12}	100^{+0}_{-12}
$4 < S_{FIRST} < 5$ mJy	17	–	–	100^{+0}_{-13}	100^{+0}_{-13}
All sources	216 (6)	28	14 (3)	89^{+2}_{-3}	94^{+2}_{-2}

Note. The number within brackets represents the number of sources flagged in the FIRST catalogue.
The errors on the completeness and reliability represent the 1σ Poissonian errors.

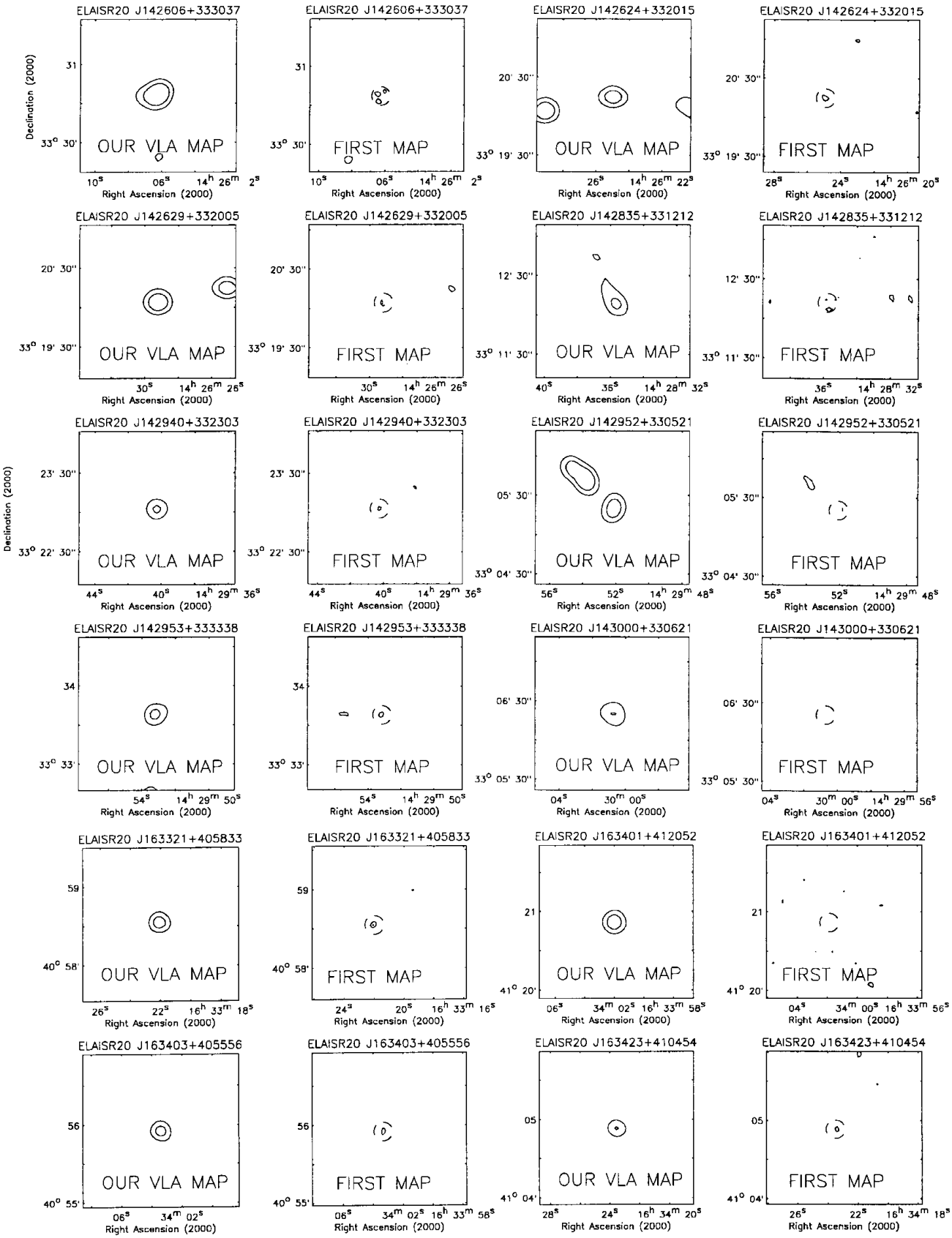

Figure 24. Contour plot of the 28 sources detected in our VLA survey with a peak flux density $S_P > 1$ mJy but not present in the FIRST catalogue. The dashed circle shows the position of the source detected in our VLA survey. All the maps have a size of 2×2 arcmin^2 and a contour levels of 0.5, 1, 2, 4, 8, 16 mJy.

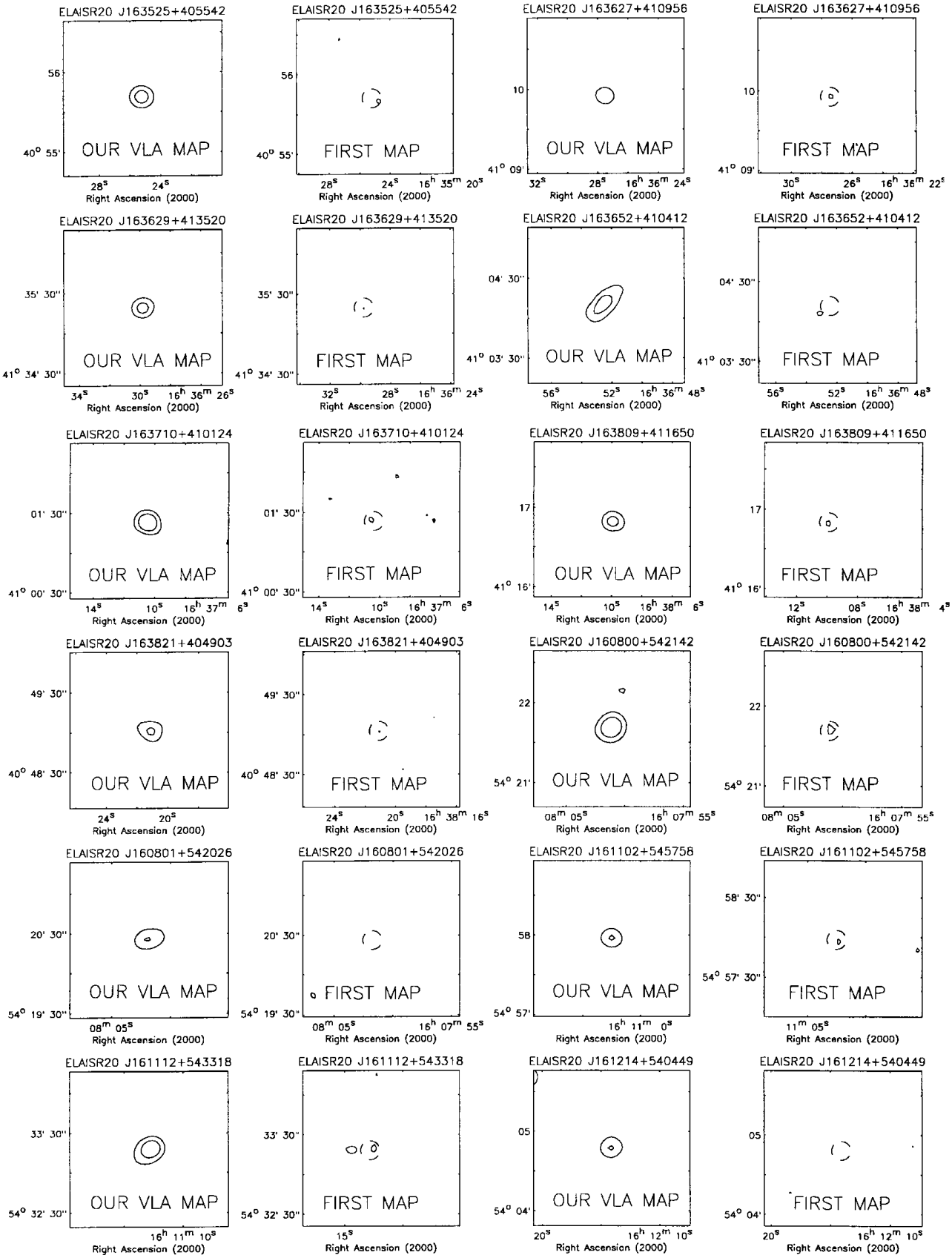

Figure 24 – *continued*

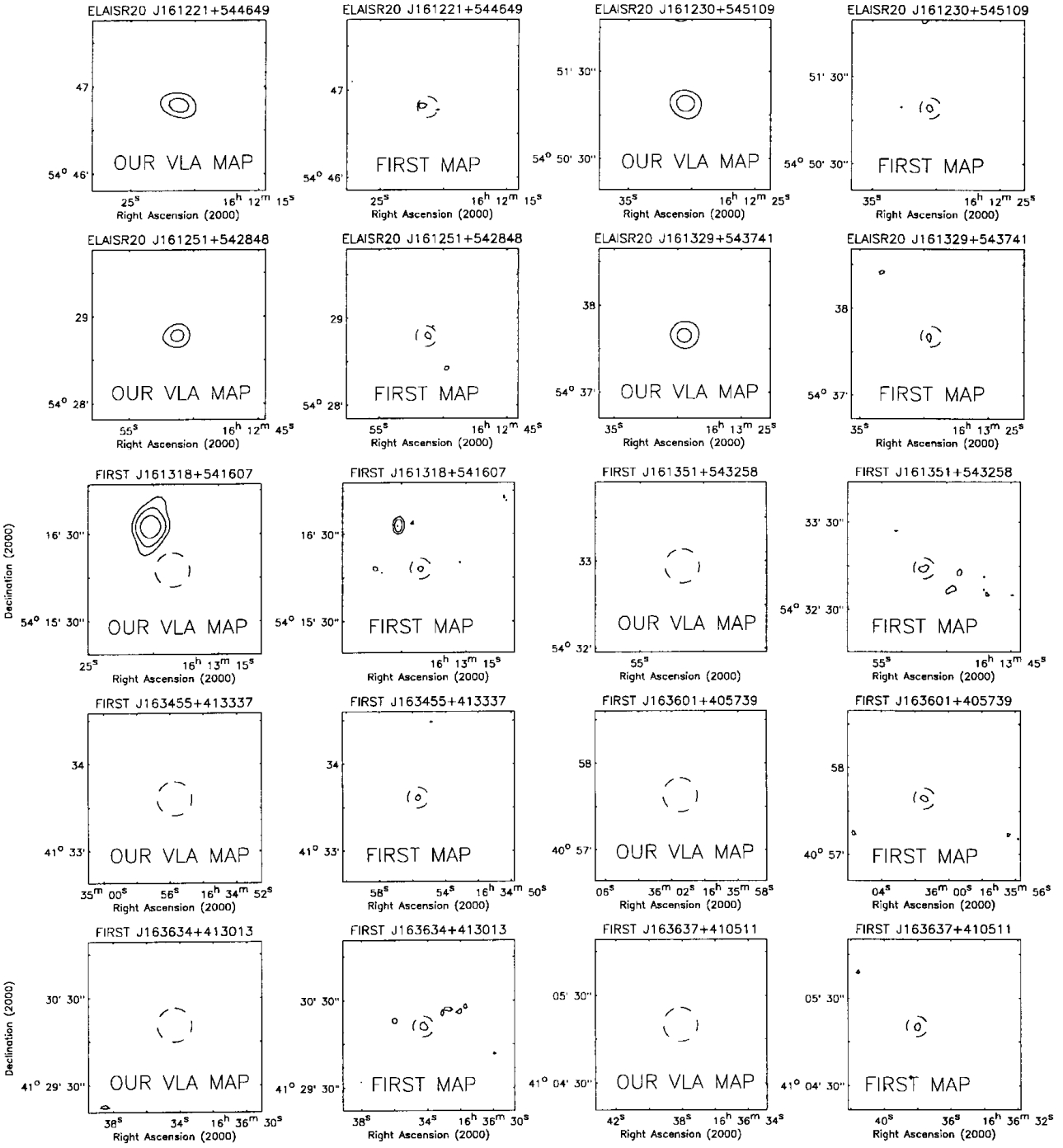

Figure 25. Contour plot of the 14 FIRST sources not in our VLA catalogue. The dashed circle shows the position of the FIRST source. All the maps have a size of 2×2 arcmin^2 and contour levels of 0.5, 1, 2, 4, 8, 16 mJy. The three sources marked with the asterisk are the sources flagged in the FIRST catalogue as possible sidelobes of a nearby bright source.

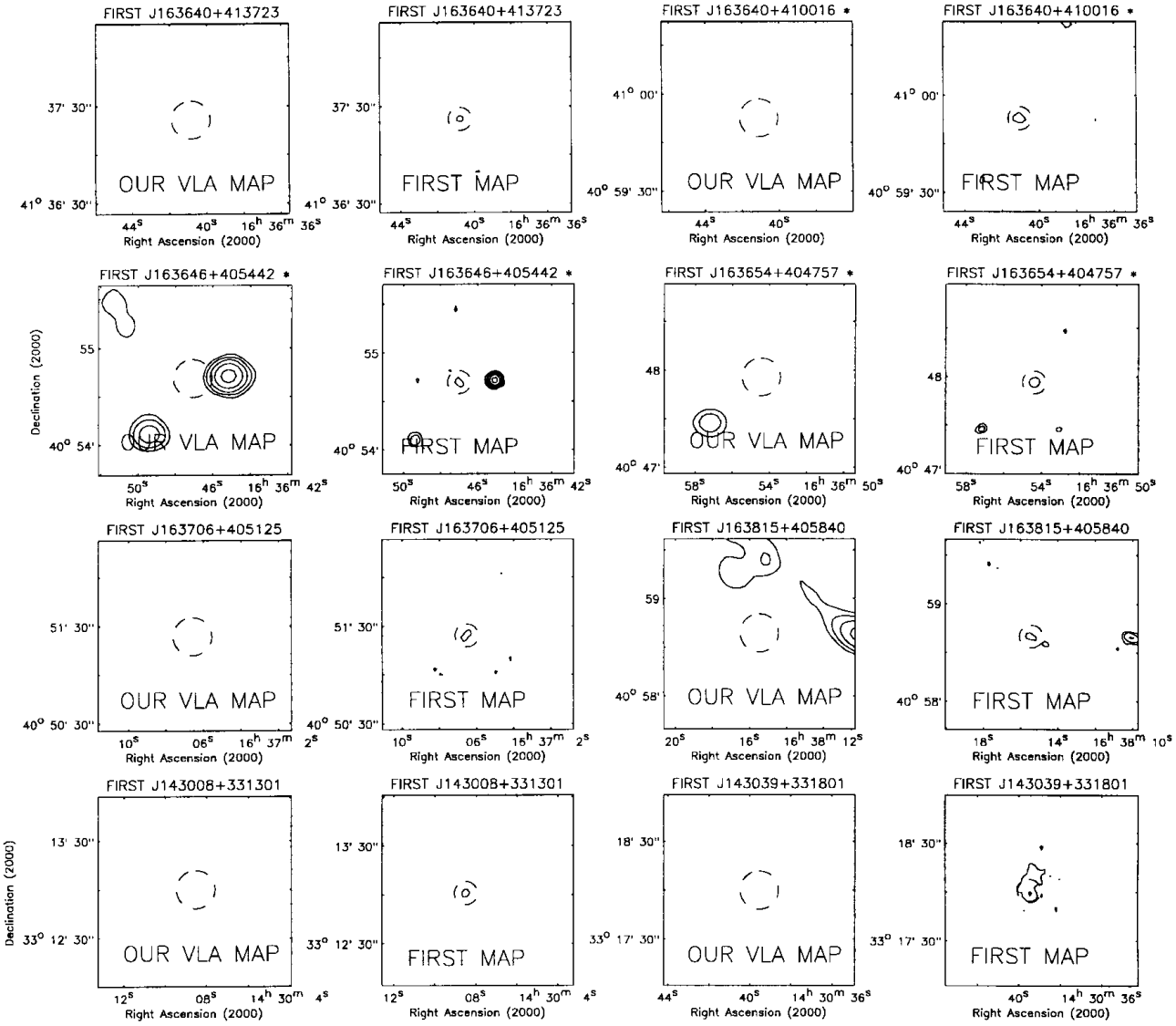

Figure 25 – *continued*